CHAPTER IV

RESULTS AND DISSCUSSIONS

4.1 Characterization of raw materials

4.1.1 Chemical compositions of raw materials

Table 4.1 The chemical compositions of raw materials

Oxides	wt (%)		
	Zn-waste	Clear cullet	Amber cullet
SiO_2	26.36	70.63	69.75
Na_2O	-	15.23	12.47
K_2O	0.82	0.28	0.09
CaO	9.79	6.96	10.77
MgO	0.84	4.32	3.05
ZnO	7.83	-	0.008
Al_2O_3	4.22	1.62	2.04
Fe_2O_3	6.62	0.08	0.32
P_2O_5	0.11	0.02	0.03
SO_3	26.37	0.09	-
TiO_2	0.17	0.07	0.13
MnO	0.56	0.02	-
CuO	0.18	-	-
As_2O_3	0.06	-	-
CdO	0.06	-	-
PbO	0.87	-	-
SnO_2	-	0.65	-
Cr_2O_3	-	-	0.009
L.O.I	15.26	-	-

The chemical compositions of Zn-waste, clear cullet, and amber cullet used in this study were determined by XRF are reported in Table 4.1. Zn-waste composed of SiO_2, CaO, ZnO, Fe_2O_3, Al_2O_3, and SO_3 as the main constituents and a small amount of ecological risky oxides such as PbO, As_2O_3, and CdO. Comparing with Zn-waste used in previous studies, the compositions of Zn-waste was varied from batch to batch [1,2]. The different in compositions of Zn-waste were a result of using different starting ore in the zinc refinery process, however, the variation of chemical compositions in each batch were small when compared with zinc hydrometallurgy waste from Europe which composed of higher amount of Fe_2O_3 (~49.3 wt%) [6].

The chemical compositions of clear and amber cullets were typical soda-lime silicate glass system. The CaO and Fe_2O_3 content in amber cullet are higher than that of clear cullet. The Fe_2O_3 is responsible for amber color of this cullet.

4.1.2 Visual observation

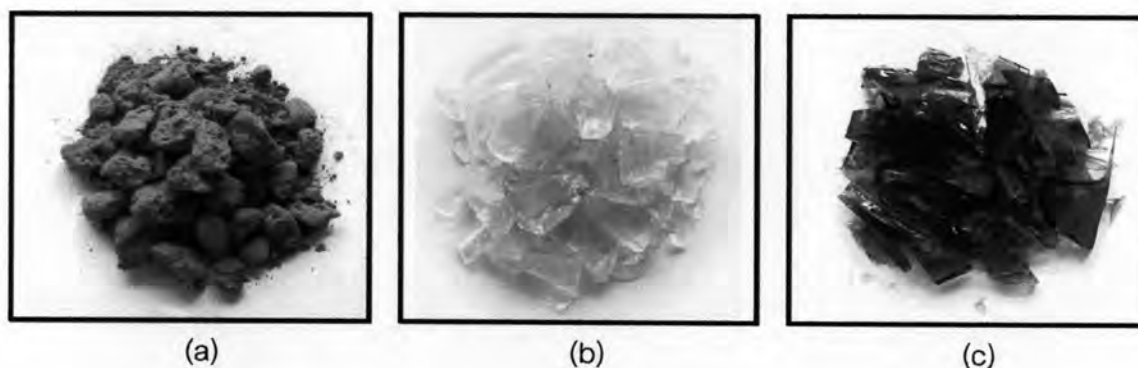(a)   (b)   (c)

Fig. 4.1 Photographs of raw materials Zn-waste (a), clear cullet (b), and amber cullet (c)

Appearance of raw materials in this study before transform to glass- ceramics are shown in Fig. 4.1. It was found that fine particle of Zn-waste from Tak plant is red-brown agglomerated. Clear cullet (float glass from Thai Asahi Co., Ltd.) is colorless and homogeneous. Amber cullet (bottles) shows amber color and homogeneous. All of the raw materials were crushed to fine particles for characterization and transformation to glass-ceramic materials in the next step.
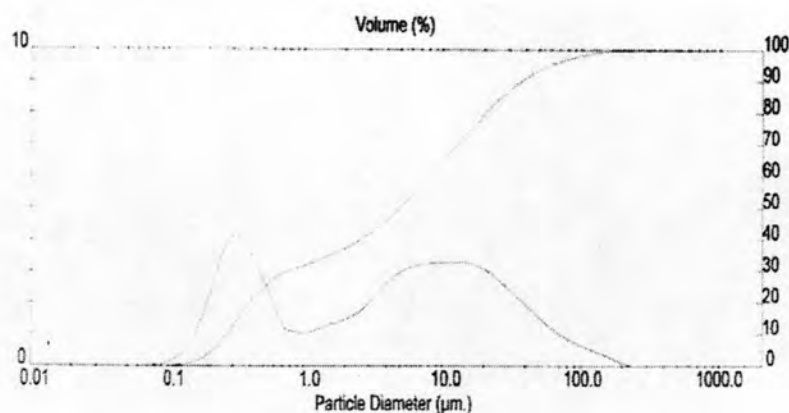
4.1.3   Particle size distribution

Fig. 4.2 Particle size distribution of Zn-waste

The particle size distribution of Zn-waste ranges from 0.05 to 222.28 µm and the average size is 13.84 µm (Fig. 4.2). It was found that particle size of this waste is very small. Therefore, it is easy to disperse in air when Zn-waste was disposed in land-filled sites. This is harmful to health and result in air pollution. In order to solve this problem, recycling Zn-waste to stable materials was studied.

4.1.4   Thermal behavior

In order to determine the thermal effect of the original Zn-waste from Tak plant for this work, differential thermal analyzer was used. From the DTA traces in Fig. 4.3, the first endothermic reaction is at the temperature about 289°C due to volatile water and other volatile matter in the structure. The second endothermic peak took place at 755°C, it is expected that endothermic reaction was occurred due to the decomposition of sulphate compounds. This is consistent with the previous study of Pelino which shown that $FeSO_4$ and $ZnSO_4$ were decomposed at temperature above 700°C [6].
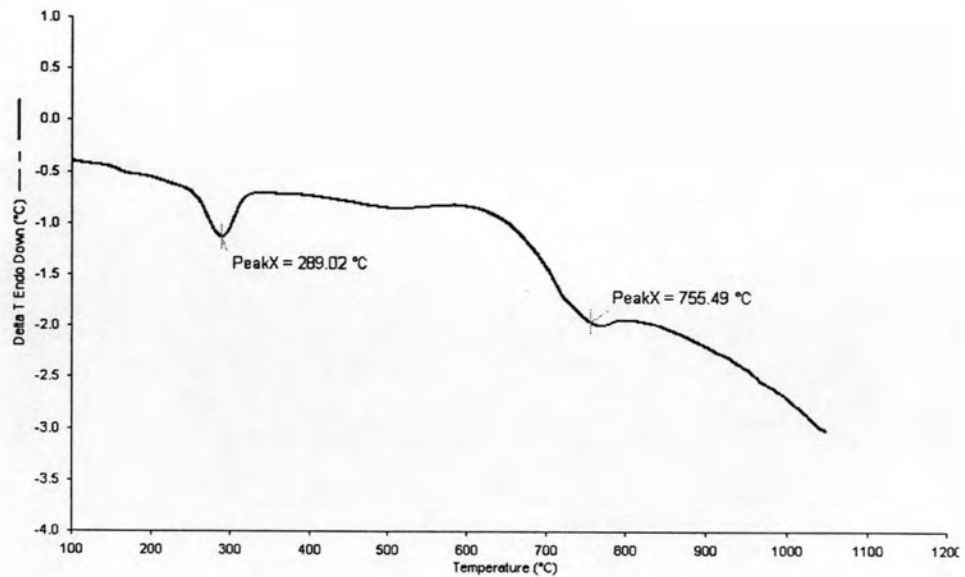
Fig. 4.3 DTA curve of Zn-waste

4.1.5 Phases formation

The major phases of Zn-waste were investigated by XRD. It was found that Quartz (SiO_2), Anhydrite ($CaSO_4$), Cristobalite (SiO_2), Willemite (Zn_2SiO_4), and Iron Oxide Hydroxide ($FeO(OH)$) were the major phases. The XRD pattern of Zn-waste is shown in Fig. 4.4.

Q = Quartz   A = Anhydrite   C = Cristobalite   W = Willemite   Fe = Iron Oxide Hydroxide
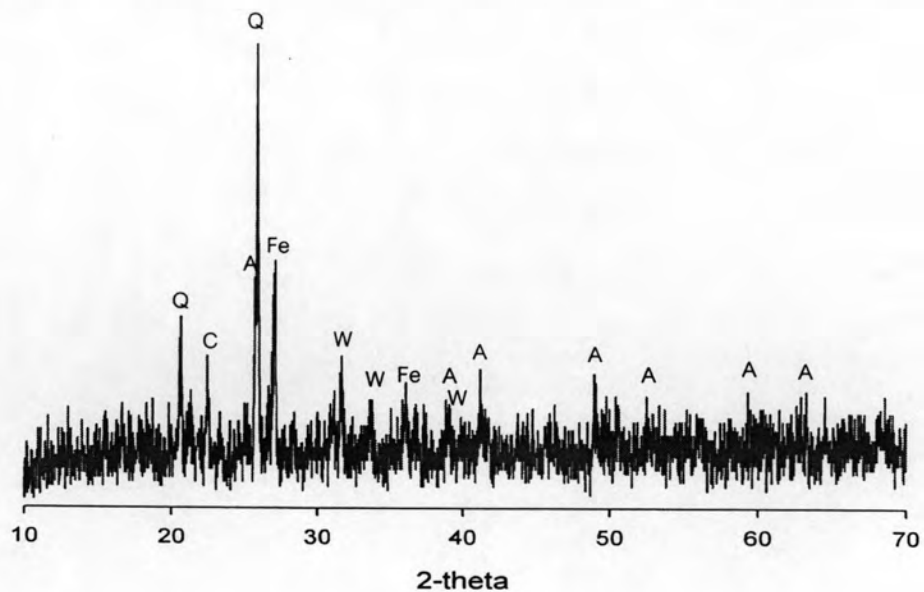

Fig. 4.4 XRD pattern of Zn-waste

4.2 Characterization of glass-ceramics obtained by non-melting process

In order to save economic loss from thermal process, preparation glass-ceramics by non-melting process was attempted. Zn-waste in the proportion of 10-90% by weight and clear cullet were mixed, pressed, and sintered. The effect of different particle size of the raw materials on physical properties was also studied.

4.2.1 Physical properties

a) Visual observation

Glass-ceramics made from coarse powders (~150 μm) and that fine powders (~44 μm) after sintering at 1000°C, 1050°C, and 1100°C for 2 hours are shown in Fig. 4.5 and Fig. 4.6, respectively. The samples were varied from a mixture of 10 wt% of Zn-waste at the left side and increased of the amount of Zn-waste to the right side of photo.
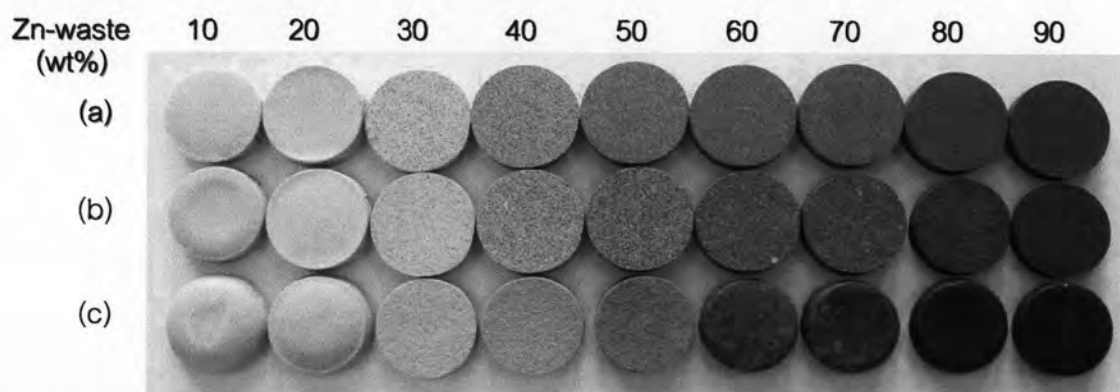

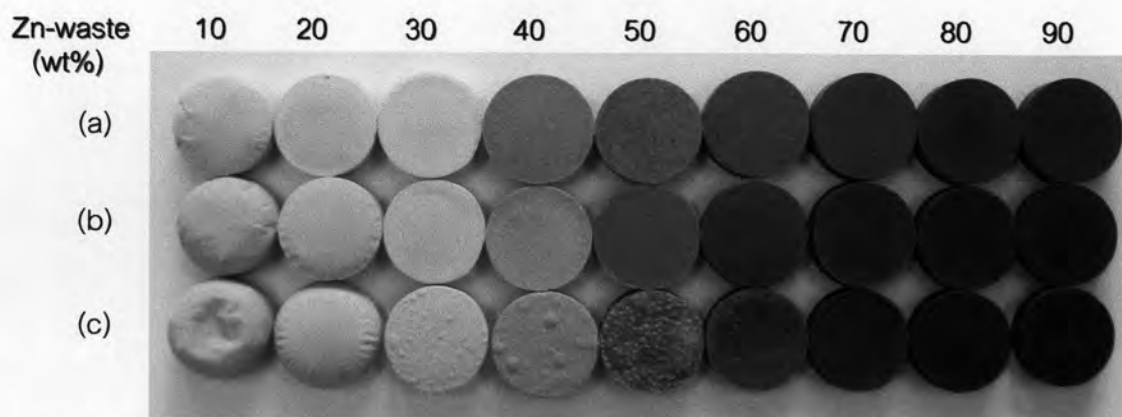Fig. 4.5 Glass-ceramics made from coarse powders sintered at 1000°C (a), 1050°C (b), and 1100°C (c)

Fig. 4.6 Glass-ceramics made from fine powders sintered at 1000°C (a), 1050°C (b), and 1100°C (c)

It can be seen that colors of glass-ceramics depend on the proportions of Zn-waste, the more percent weight of Zn-waste mixed, the darker brown of samples occurred. Intense color was due to an increasing amount of Fe_2O_3 in Zn-waste. It is in good agreement with work of Donald, et al. [25], brown color was occurred in frit as the result of adding Fe_2O_3 greater than 3 wt%.

The surfaces of glass-ceramics made from coarse powders were rougher than the one made from fine powders in every sintering temperature. Independent on the size of starting powders, samples which have the ratio of Zn-waste less than 30 wt% were deformed after sintering at $1050^{\circ}C$. Beside, it can be observed that some of the specimens made from fine powders were bloated (Fig. 4.6(c)) after sintering at $1100^{\circ}C$ because fine powders were easier reacted than coarse powders. Thus, specimens contained high amount of glass and lime in starting Zn-waste were bloated caused some gas entrapment.

b) <u>Apparent porosity, water absorption, bulk density, and volume shrinkage</u>

To evaluate the sintering behavior of glass-ceramics, physical properties for example apparent porosity, water absorption, bulk density, and volume shrinkage of glass-ceramics were determined. These properties of glass-ceramics made from coarse powders are shown in Fig. 4.7-Fig. 4.10. For glass-ceramics made from coarse powders with Zn-waste > 30 wt%, the proportions of Zn-waste have a little effect on the properties at the constant sintering temperature. Generally, apparent porosity is related with water absorption, namely higher apparent porosity, higher water absorption. In Fig. 4.7, most of the specimens sintered at $1000^{\circ}C$ and $1050^{\circ}C$ showed apparent porosities higher than 30% while all of the specimens sintered at $1100^{\circ}C$ had apparent porosity less than 10%. Similarly, water adsorption of the specimens sintered at $1000^{\circ}C$ and $1050^{\circ}C$ was more than 20% and decreased to less than 5% after sintered at $1100^{\circ}C$ as seen in Fig. 4.8. Fig. 4.7 and Fig. 4.8 show that apparent porosity and water absorption decreased with the increasing in sintering temperatures.

Bulk density and volume shrinkage of samples increased with an increasing in sintering temperatures. It is clear in Fig. 4.9 and Fig. 4.10 that bulk density and volume shrinkage of samples sintered at 1100°C were higher than other temperatures and they show the relationship between bulk density and volume shrinkage. It was found that the higher bulk density as a result of the higher volume shrinkage. However, due to the deformation of samples, the specimens with 10 and 20 wt% of Zn-waste sintered at 1100°C, were not followed this valuation. The raw data of apparent porosity, water absorption, bulk density, and volume shrinkage of glass-ceramics made from coarse powders after sintering at various temperatures are shown in Appendix A.
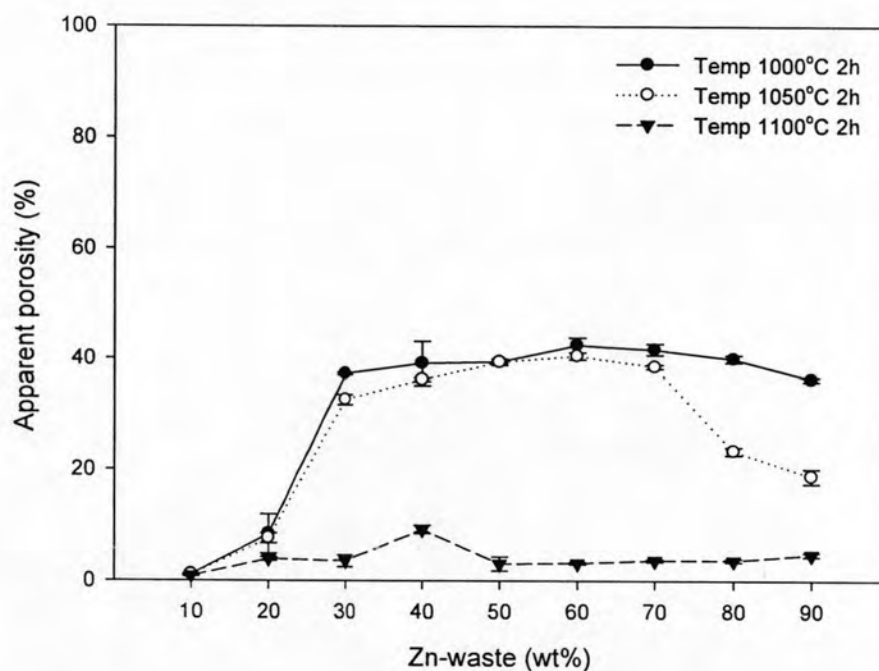

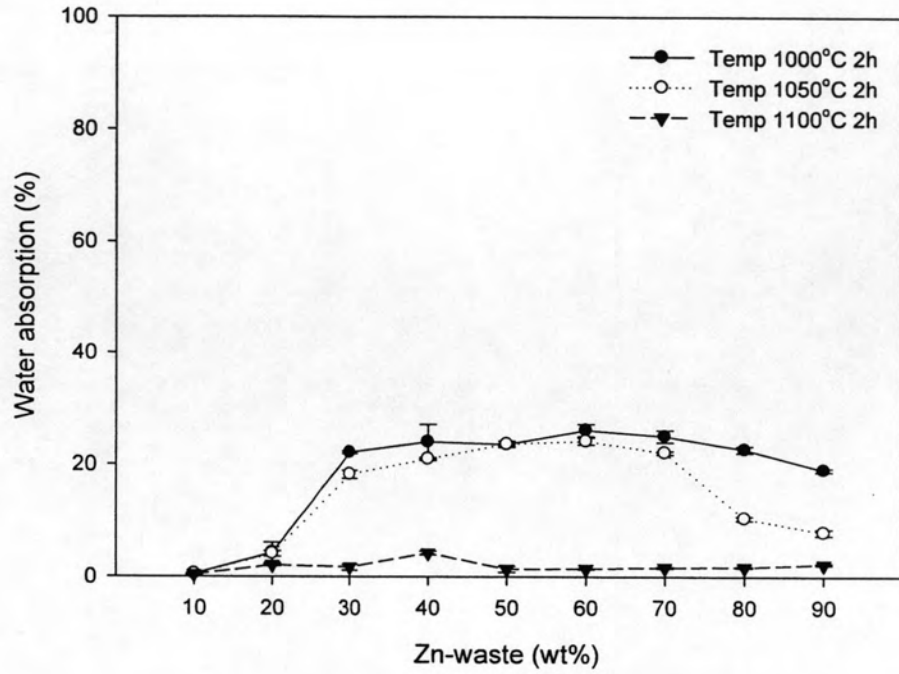Fig. 4.7 Apparent porosity of glass-ceramics made from coarse powders

Fig. 4.8 Water absorption of glass-ceramics made from coarse powders
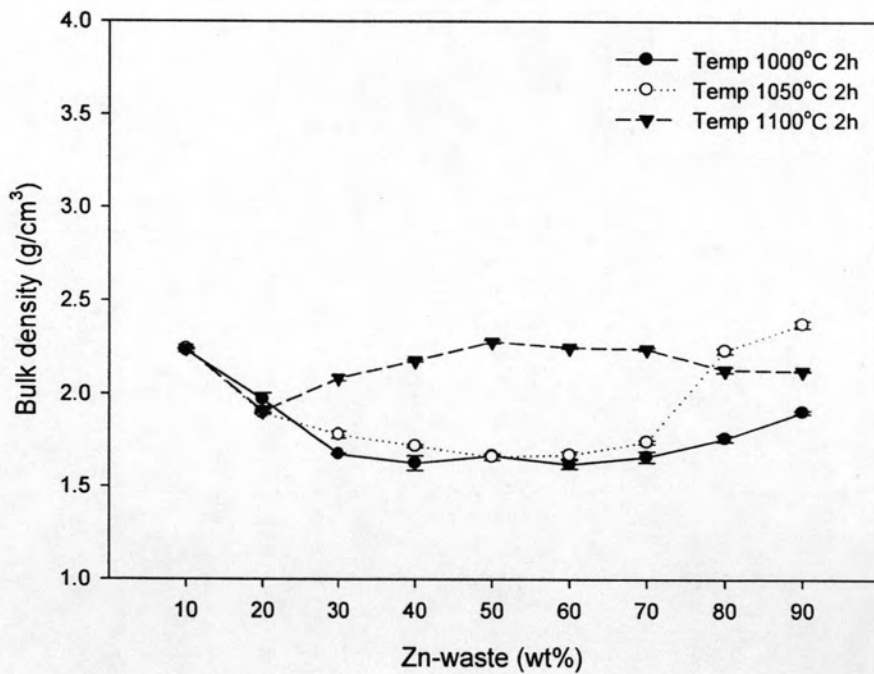

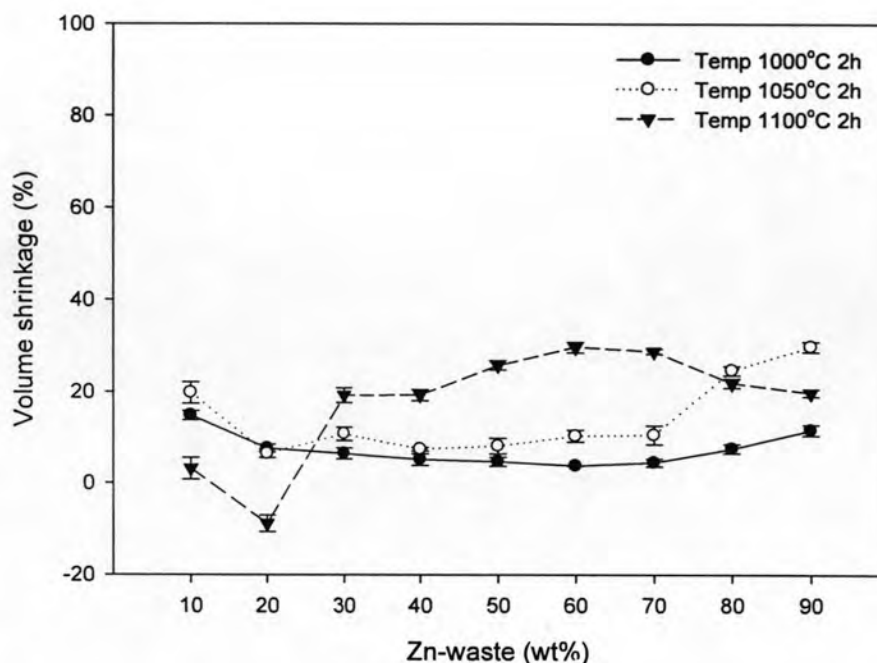Fig. 4.9 Bulk density of glass-ceramics made from coarse powders

Fig. 4.10 Volume shrinkage of glass-ceramics made from coarse powders

For glass-ceramics made from fine powder, apparent porosity, water absorption, bulk density, and volume shrinkage are shown in Fig. 4.11, Fig. 4.12, Fig. 4.13, and Fig. 4.14, respectively. The apparent porosity and water absorption of glass-ceramics made from fine powders showed the same trend as glass-ceramics made from coarse powders. They decreased, as temperatures increased. At temperatures of $1000^{\circ}C$ and $1050^{\circ}C$, the apparent porosity and water absorption of specimens made from fine powders are lower than that of the specimens made from coarse powders because fine powder can easily be sintered than coarse powder. However, this trend was not found at $1100^{\circ}C$ because the specimens were over fired and bloated at this temperature as shown in Fig. 4.6.

Bulk density of specimens made from fine powders sintered at various temperatures was not much different with specimens made from coarse powders. The specimens made from fine powders were easier to sinter than the one made from coarse powders, therefore, dense specimens can be achieved at lower sintering temperature.

The raw data of apparent porosity, water absorption, bulk density, and volume shrinkage of glass-ceramics made from fine powders after sintering various temperatures are shown in Appendix B.
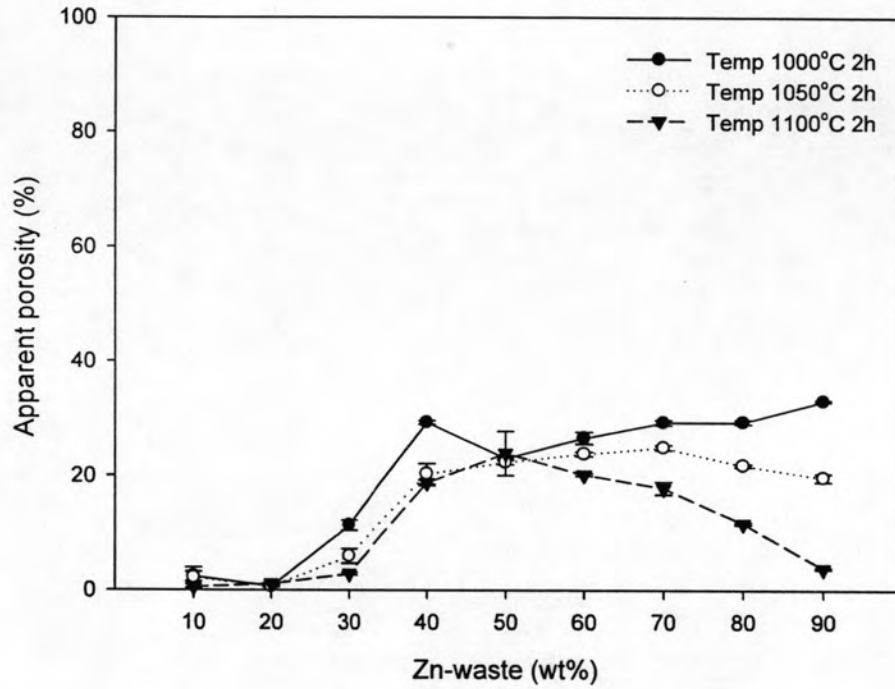

Fig. 4.11 Apparent porosity of glass-ceramics made from fine powders
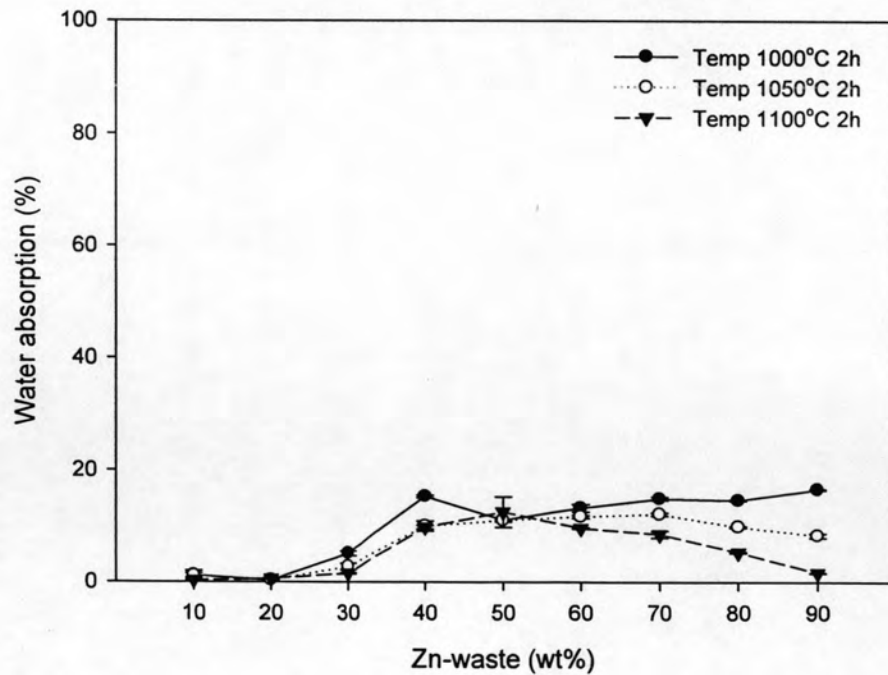

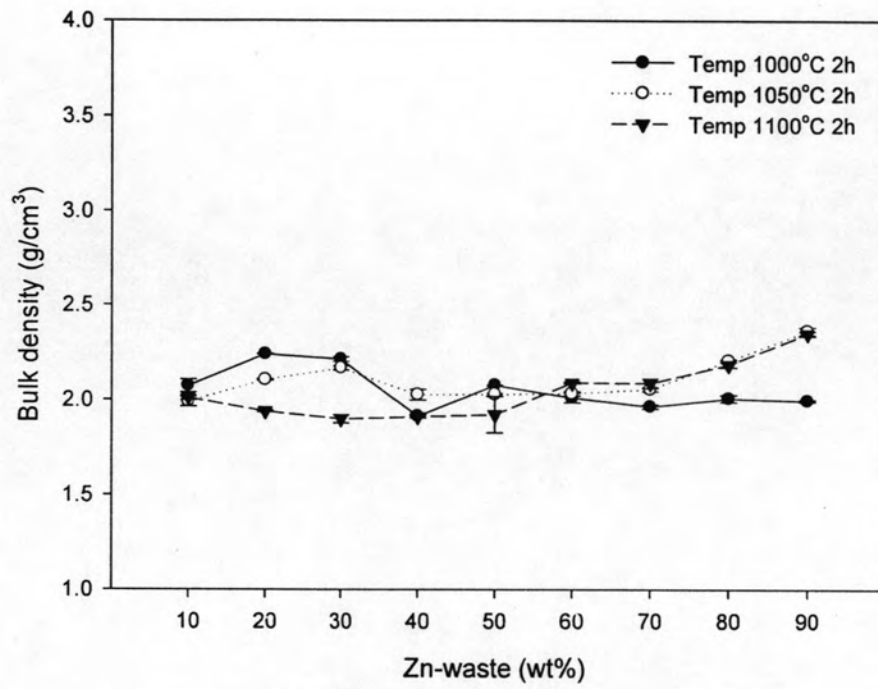Fig. 4.12 Water absorption of glass-ceramics made from fine powders

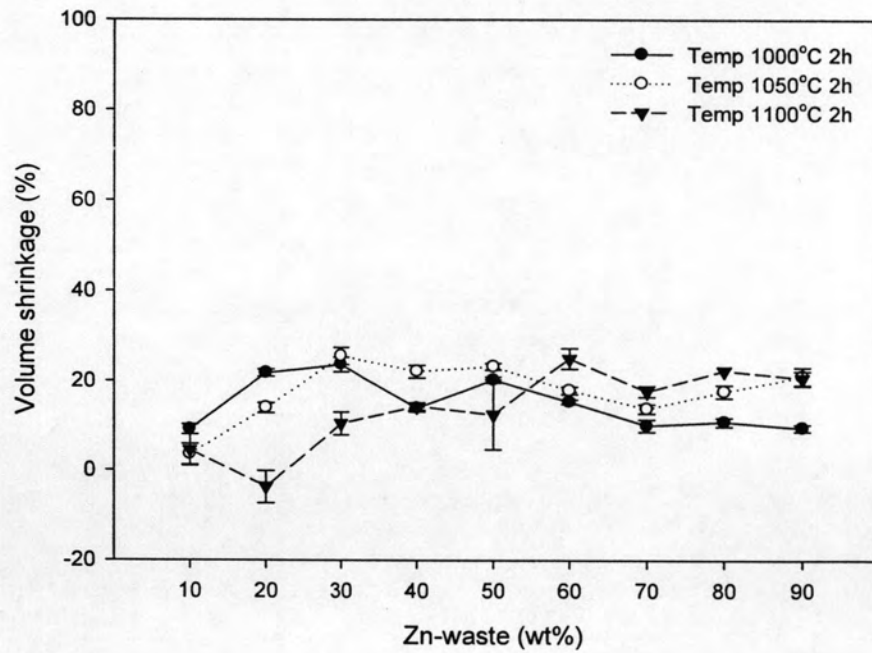Fig. 4.13 Bulk density of glass-ceramics made from fine powders

Fig. 4.14 Volume shrinkage of glass-ceramics made from fine powders

4.2.2   Porosity

Porosity has strongly influence on the strength of specimens because the cross-section area of specimens was reduced and result in easy to break when the load is applied. Thus, it is advisable to study pore features such as size and shape using optical microscope (OM). Specimens with Zn-waste of 10, 50, and 90 wt% were selected to demonstrate about effect of temperatures and percentage of Zn-waste on their microstructure. The optical micrographs of the specimens made from coarse and fine powders were compared in Fig. 4.15 and Fig. 4.16.
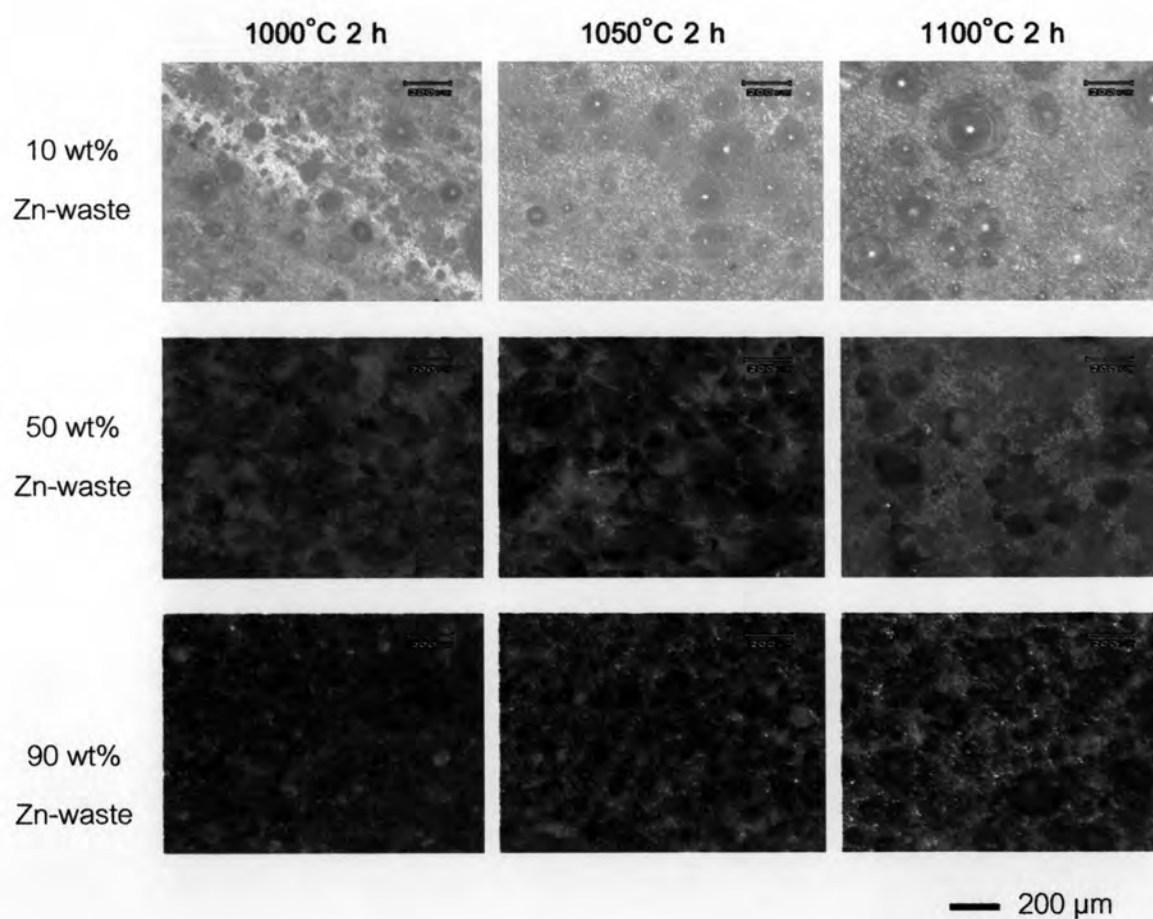

Fig. 4.15 Optical micrographs of glass-ceramics made from coarse powders

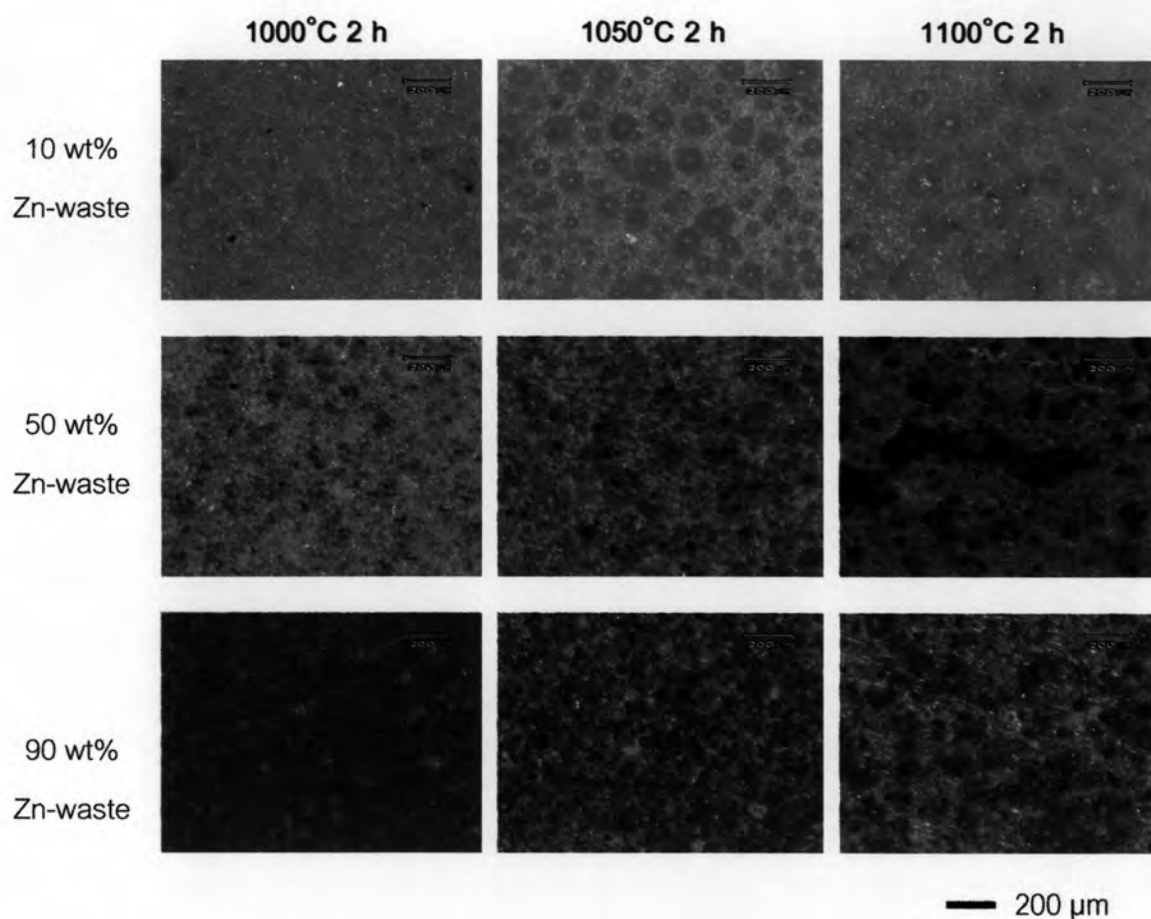| | 1000°C 2 h | 1050°C 2 h | 1100°C 2 h |
10 wt% Zn-waste			
50 wt% Zn-waste			
90 wt% Zn-waste			

— 200 µm

Fig. 4.16 Optical micrographs of glass-ceramics made from fine powders

It was found that all specimens are porous and pore size of specimens made from coarse powders was larger than that of specimens made from fine powders. These pores became larger after sintered at higher temperature because of a mechanism for materials transport in order to get densification of specimens [26]. This result was confirmed by bulk density, apparent porosity, and water absorption of the specimens as described previously. Moreover, it was also found that the higher amount of Zn-waste in specimens show smaller pore sizes and connected porous owing to the reduction of SiO_2 in chemical composition. The optical micrographs of other specimens are shown in Appendix C.

4.2.3 Bending strength

The bending strength of glass-ceramics made from coarse powders sintered at $1100^{\circ}C$ was investigated by three-point bending. They were selected because they show lower apparent porosity, lower water absorption, and the highest bulk density. In addition, Fig. 4.6 shows non-well sintered of specimens made from fine powders which will influence on mechanical properties. The bending strength of the glass-ceramics was shown in Fig. 4.17.
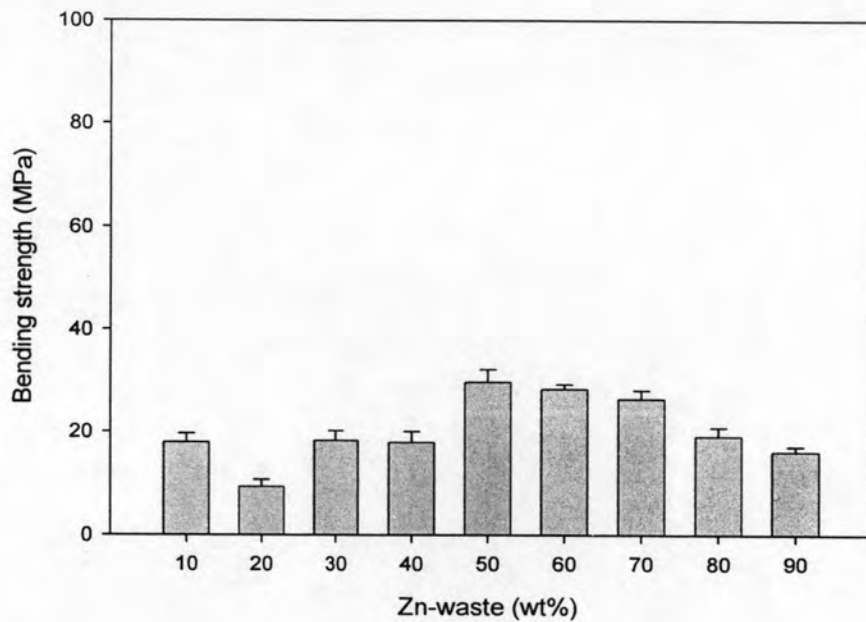

Fig. 4.17 Bending strength of glass-ceramics made from coarse powders sintered at $1100^{\circ}C$ 2 h

The maximum strength (~29.7 MPa) was found at constant 50:50 ratio of raw materials. It was also found that the bending strength was related with bulk density (Fig. 4.9), that is the highest bulk density results in the highest strength. The raw data of bending strength are shown in Appendix A.

The bending strength of these glass-ceramics was lower than general glass-ceramics because of the presence of higher porosity which have direct effect on strength. However, these strengths are sufficient and suitable for use as decorated materials.

4.3 Glass-ceramics obtained by melting and sintering process

In this process, the mixture had to vitrify prior to sintering glass powder in one step to acquire glass-ceramics. Zn-waste was mixed with each cullet (clear and amber cullet) in the proportion as shown in Table 4.2. To obtain parent glasses, the mixtures were melted at $1450^{\circ}C$ for 1 hour in an alumina-zircon crucible. The viscosity, homogeneity, and color after melting of glasses were investigated.

Table 4.2 Proportion of investigated samples

Samples	Raw materials (wt%)		
	Zn-waste	clear cullet	amber cullet
100C	0	100	0
2Z8C	20	80	0
4Z6C	40	60	0
6Z4C	60	40	0
100A	0	0	100
2Z8A	20	0	80
4Z6A	40	0	60
6Z4A	60	0	40
100Z	100	0	0

4.3.1　Characterization of parent glasses

4.3.1.1　Physical properties

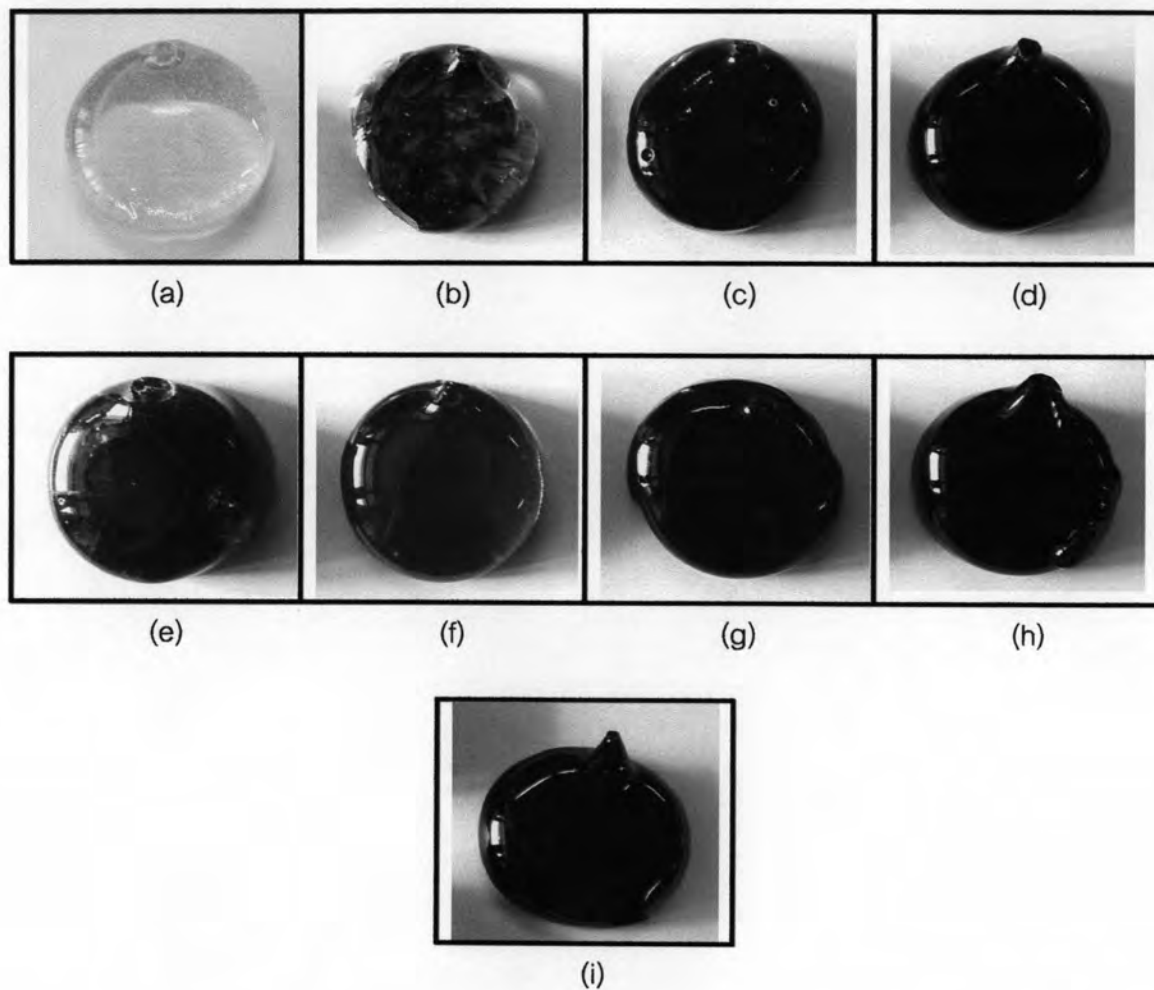a)　<u>Visual observation</u>

Fig. 4.18 Parent glasses of 100C (a), 2Z8C (b), 4Z6C (c), 6Z4C (d), 100A (e), 2Z8A (f), 4Z6A (g), 6Z4A (h), 100Z (i)

All molten glasses were homogeneous and their viscosities increased with an increase in the amount of Zn-waste and this was accordance with the percentage of SiO_2 in the composition [27]. The photographs of 100C, 2Z8C, 4Z6C, 6Z4C, 100A, 2Z8A, 4Z6A, 6Z4A, and 100Z were shown in Fig. 4.18. The color of the glasses changed from light green to dark green, as the percentage of Zn-waste increased and nearly become black in 100Z (Fig. 4.18(i)).
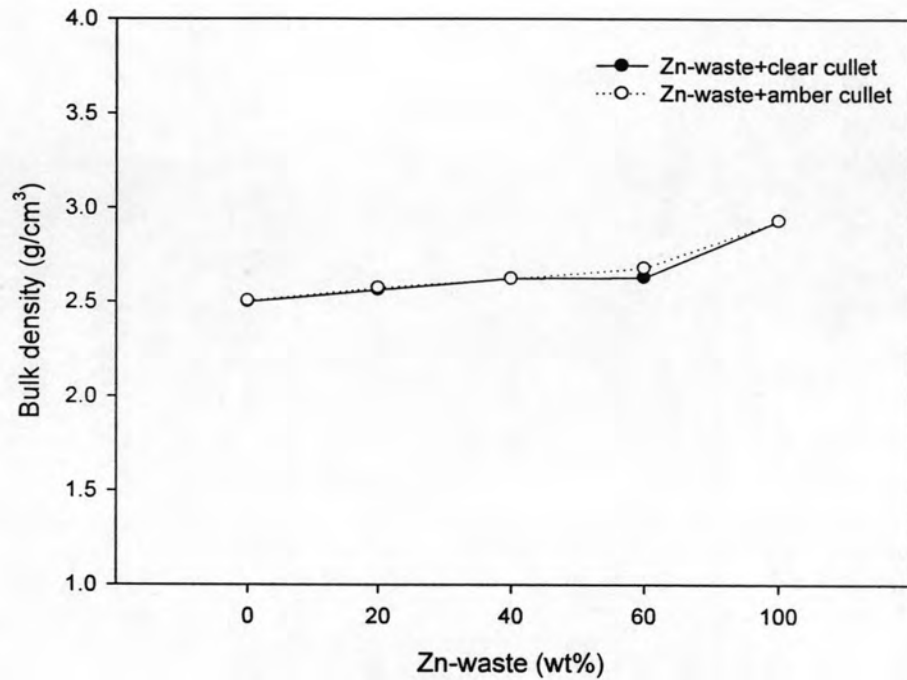
b) <u>Bulk density</u>

Fig. 4.19 Bulk density of glasses melted at $1450^{\circ}C$ for 1 hour

Bulk density of molten glasses increased with increasing the amount of Zn-waste as shown in Fig. 4.19. It was found that bulk density of both glasses with clear cullet and amber cullet, increased from 2.5 to 2.93 g/cm^3 as the proportion of Zn-waste increased from 0 to 100 wt%.

4.3.1.2 Thermal behavior

To investigate glass transition temperature (T_g) and crystallization temperature (T_c) of glasses, differential thermal analysis (DTA) was used followed ASTM E 1356 03 [28]. T_g was estimated from first base line deviation and T_c was extrapolated from onset temperature using computer software [29]. An example of estimation of T_g and T_c of glass 100A was given in Fig. 4.20. It is illustrated that T_g and T_c were about $570^{\circ}C$ and $798^{\circ}C$, respectively.
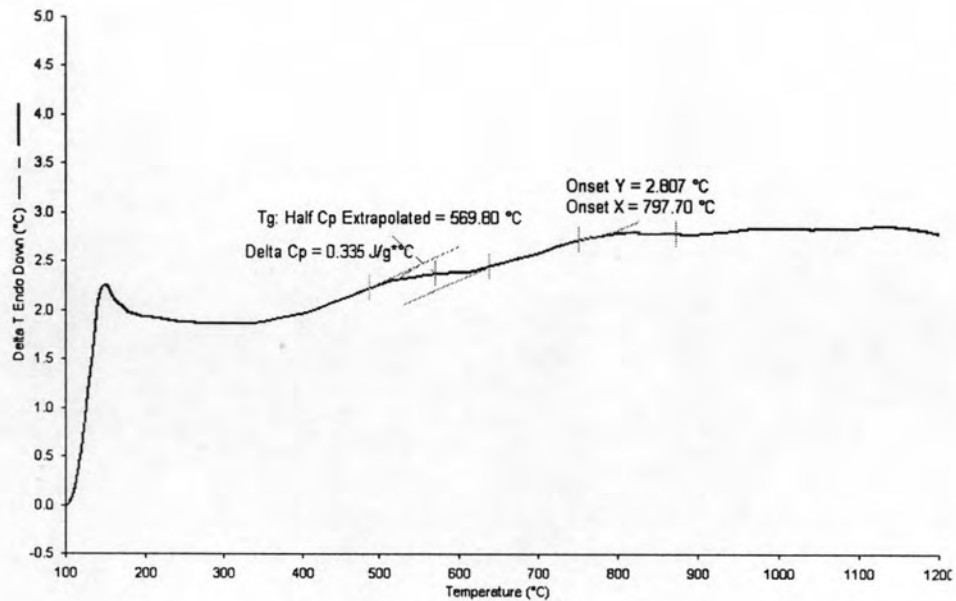
Fig. 4.20 DTA curve of 100A glass

Results of T_g and T_c of all samples are shown in Table 4.3. It was found that values of T_g and T_c range from 562-627°C and 771-895°C, respectively. The values of T_g and T_c of most glasses were likely to increased with a decreasing in proportional of alkali oxides in the composition. From crystallization temperature (T_c), two sintering temperatures, 750°C and 850°C, are chosen in order to study the effects of the sintering temperatures on final properties of glass-ceramics.

Table 4.3 Thermal analysis results from DTA

Samples	T_g ($^\circ$C)	T_c ($^\circ$C)
100C	562	771
2Z8C	557	790
4Z6C	618	782
6Z4C	627	879
100A	570	798
2Z8A	622	811
4Z6A	616	840
6Z4A	627	778
100Z	-	895

4.3.1.3 Thermal expansion coefficient

Thermal expansion coefficient in the range of 35-350°C are shown in Fig. 4.21. It was found that thermal expansion coefficient decreased with increasing in content of Zn-waste.
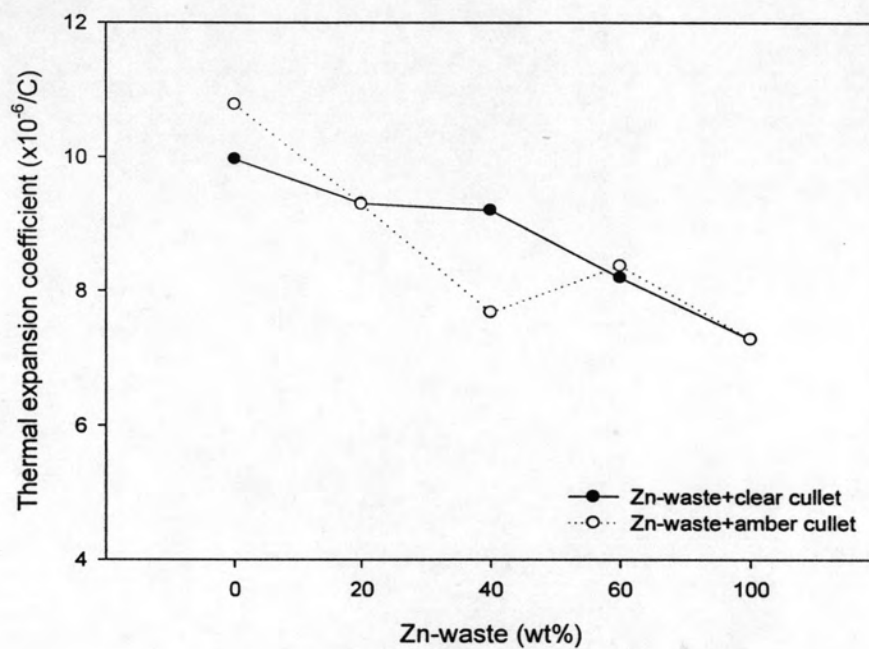

Fig. 4.21 Thermal expansion coefficient of parent glasses

4.3.2　Characterization of glass-ceramics

After melting, parent glasses were ground in order to get a fine powder then glass powders were pressed into a bar shape and subsequently sintered at 750°C and 850°C for 2 hours.

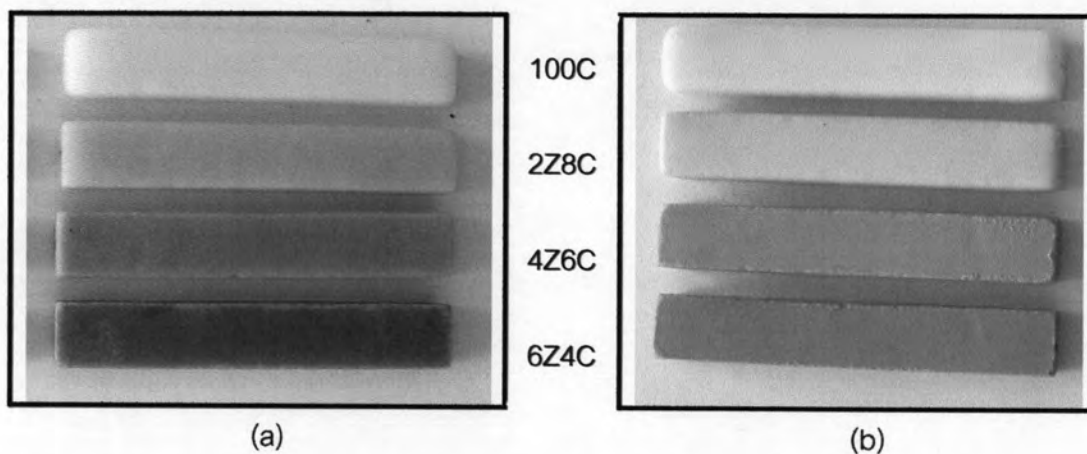### 4.3.2.1　Physical properties

a) <u>Visual observation</u>

(a)　　　　　　　　　　　　　　　　(b)

Fig. 4.22 Glass-ceramics from Zn-waste mixed with clear cullet sintered at 750°C (a) and 850°C (b)
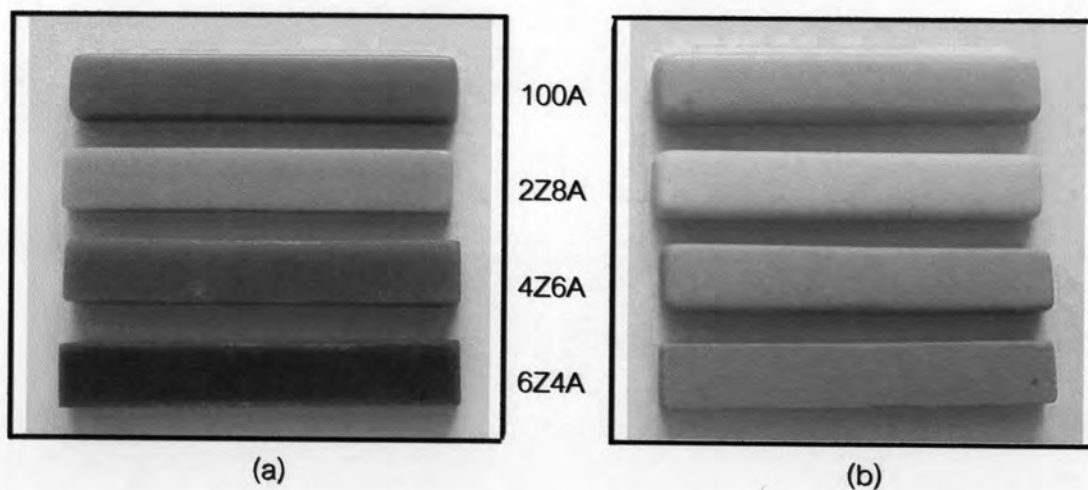

(a)　　　　　　　　　　　　　　　　(b)

Fig. 4.23 Glass-ceramics from Zn-waste mixed with amber cullet sintered at 750°C (a) and 850°C (b)

After sintering at 750°C and 850°C, shapes, surfaces, and colors of glass-ceramics were observed. Fig. 4.22 and Fig. 4.23 show the photographs of sintered materials. Glossy surface was occurred after sintered at 750°C and changed to matt surface after sintered at 850°C. The color of glass-ceramics was change from their parent glasses, for example the color of 4Z6C, 6Z4C, 4Z6A, and 6Z4A transfers from green color to brown color after sintering. Sufficient amount of Fe_2O_3 in composition of 4Z6C, 6Z4C, 4Z6A, and 6Z4A resulted in oxidation from the presence of oxygen in air of ferrous ions, Fe^{2+} to ferric ions, Fe^{3+}. Iron prefers to be in the more stable Fe^{3+} rather than the Fe^{2+} state. This oxidation state has the characteristic of yellowish-brown color [25].

When Zn-waste was added in the mixtures, the color shades of glass-ceramics were also changed from white (100wt% clear cullet) and yellowish brown (100wt% amber cullet) color to green and brown color. The colors of glass-ceramics depend on the composition and sintering temperature.

b) Shrinkage

Shrinkages of glass-ceramics were evaluated both linear shrinkage and volume shrinkage by measurement size of samples before and after firing as shown in Fig. 4.24.
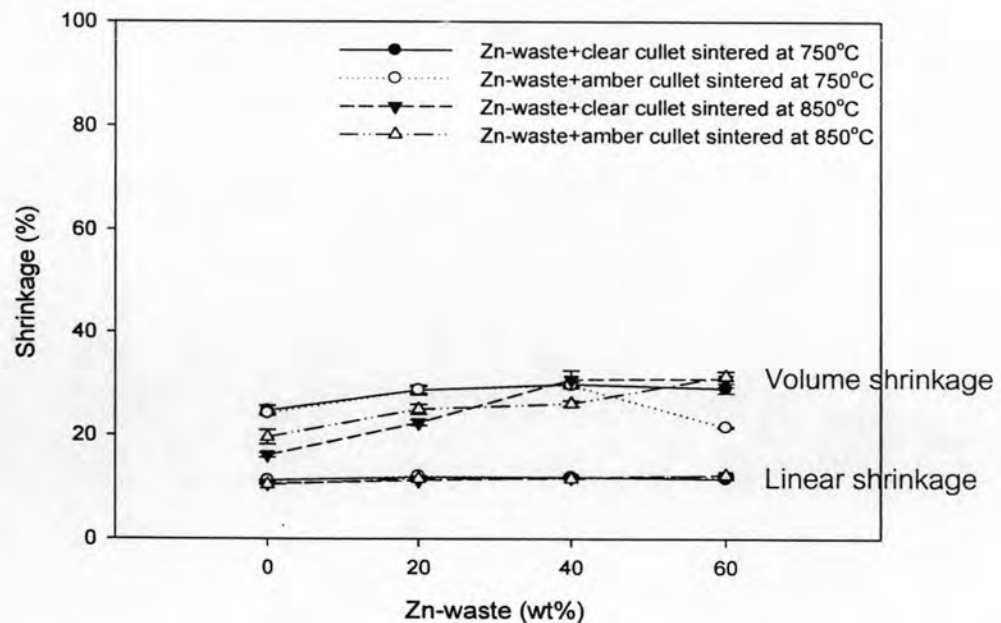

Fig. 4.24 Linear and Volume shrinkage of glass-ceramics

Linear shrinkage of glass-ceramics which measured from length of samples was about 10% and it was not depend on sintering temperatures and the amount of Zn-waste. For volume shrinkage, sintering temperatures and composition of Zn-waste had a little effect on volume shrinkages of samples. Normally, the value of isotropic volume shrinkage is about three times of the linear shrinkage but in this investigation was found that glass-ceramics added Zn-waste in quantities up to 40 wt%, the volume shrinkage was less than three times of the linear shrinkage. It is possible that specimens were anisotropic volume shrinkage owing to different change in dimension in each direction.

c) Apparent porosity, water absorption, and bulk density

All glass-ceramics had percent of apparent porosity and water absorption near 0% as shown in Fig. 4.25 and Fig. 4.26, respectively.
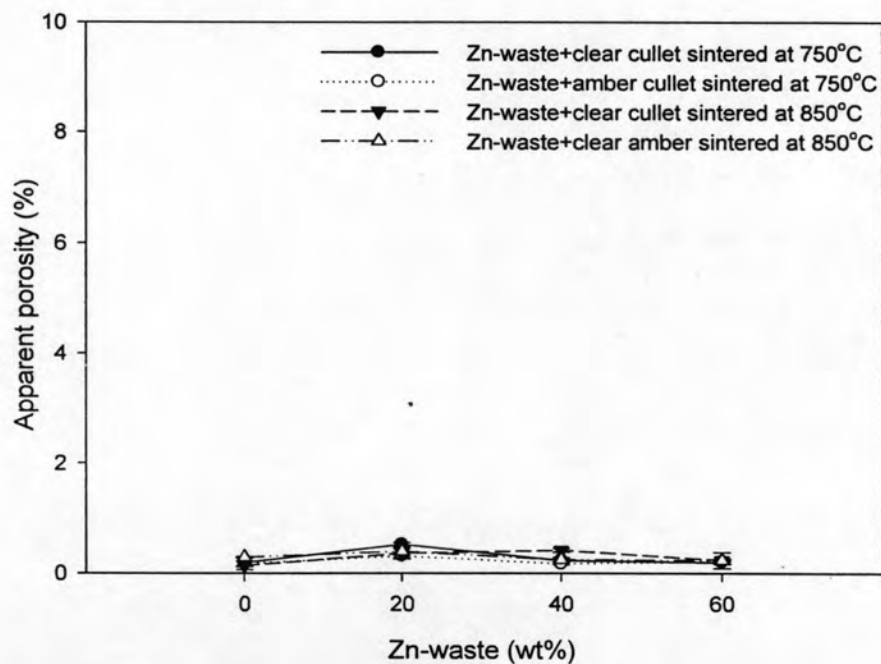
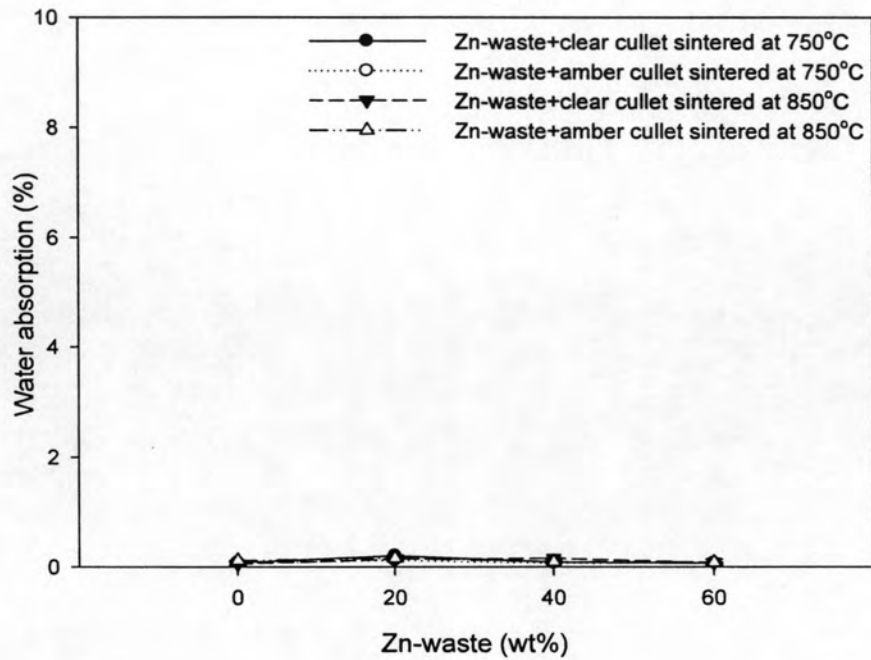Fig. 4.25 Apparent porosity of glass-ceramics

Fig. 4.26 Water absorption of glass-ceramics

It is believed that the decreasing of percent water absorption and percent apparent porosity after sintering is the result of the elimination of opened pores. The near zero water absorption is represented that most of the opened pores in glass-ceramics were completely removed after heat-treatment.
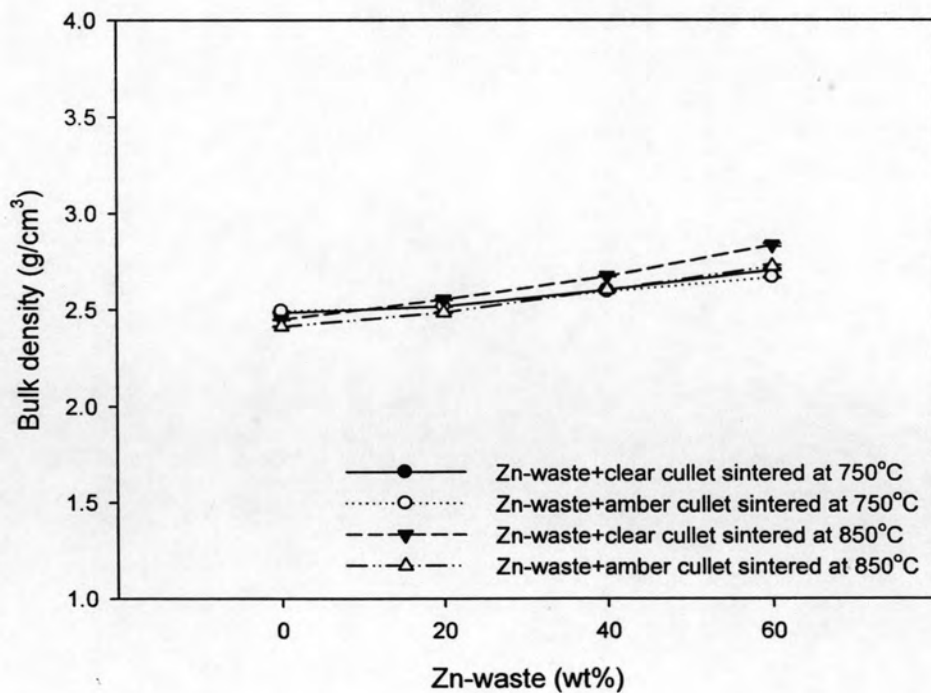

Fig. 4.27 Bulk density of glass-ceramics

Bulk density of each specimen was individual characteristic but for the similar materials, densities were able to vary with structures, porosities, and compositions. In case of this study, bulk density of sintered specimens is shown in Fig. 4.27. It was found that bulk density of glass-ceramics contained Zn-waste and clear cullet sintered at 750°C and 850°C were in the range of 2.48-2.70 g/cm³ and 2.45-2.83 g/cm³, respectively. For glass-ceramics contained Zn-waste and amber cullet sintered at 750°C and 850°C, bulk densities were 2.45-2.83 g/cm³ and 2.41-2.72 g/cm³. It is clearly that bulk density of glass-ceramics varied as a function of percent Zn-waste and their density was higher than the parent glass (Fig. 4.19). The effect of types of cullet on bulk density was not clear in this study. Besides, shrinkages during heat-treatment were also affected on density due to loss of compositions and combinations of interior structure were occurred. As seen in Fig. 4.24 and Fig. 4.27, the more percent volume shrink, the higher bulk densities get. The raw data of shrinkages, apparent porosity, water absorption, and bulk density of glass-ceramics showed in Appendix D.

4.3.2.2 Phase formation

Crystalline formation of glass-ceramics was analyzed by XRD [30]. For glass-ceramics contained Zn-waste and clear cullet, the XRD patterns of the specimens heat-treated at 750°C and 850°C are shown in Fig. 4.28 and Fig. 4.29, respectively. All of the specimens sintered at 750°C show an amorphous pattern but after heat-treatment at 850°C, crystalline phases occurred as mixed phases, i.e. cristobalite (SiO_2), diopside ($CaMgSi_2O_6$), wollastonite ($CaSiO_3$), and esseneite, sodian ($(Ca,Na)(Fe,Mn,Zn)Si_2O_6$). It was found that different crystalline phases present in each glass-ceramics depending on the glass-ceramics compositions. That is, the XRD pattern of 100C illustrates peak intensities corresponding to cristobalite (SiO_2), diopside ($CaMgSi_2O_6$), and wollastonite ($CaSiO_3$). In 2Z8C and 4Z6C glass-ceramics, only the peak of wollastonite ($CaSiO_3$) was gradually disappeared but cristobalite (SiO_2) and diopside ($CaMgSi_2O_6$) phases remained in the structure. For the 6Z4C glass-ceramics, the peaks of cristobalite (SiO_2), diopside ($CaMgSi_2O_6$), and esseneite-sodian ($(Ca,Na)(Fe,Mn,Zn)Si_2O_6$), solid solution of cation in diopside structure were observed. This was closed to the XRD results of 100Z.

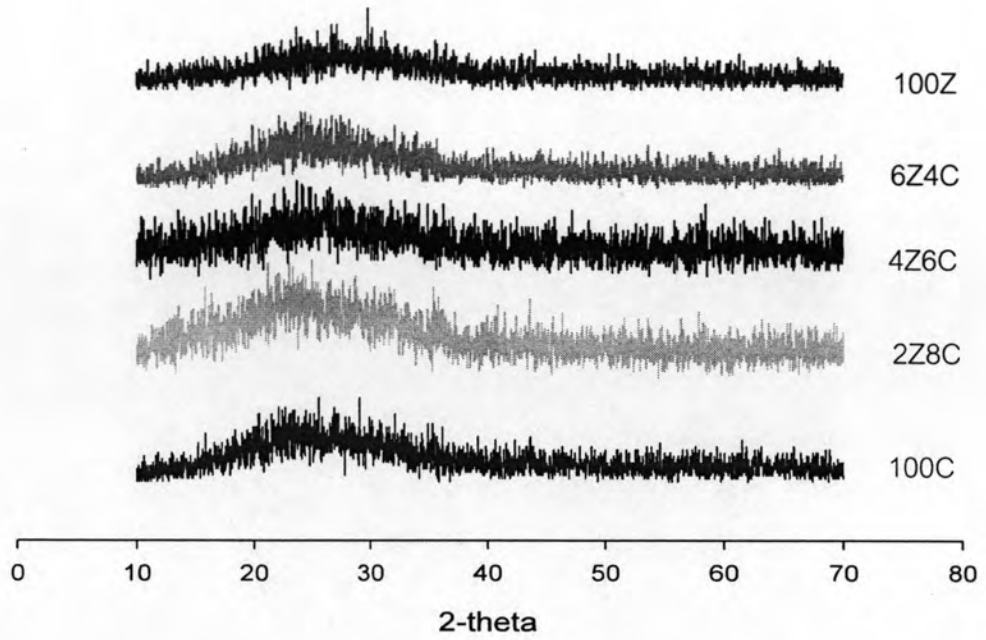Fig. 4.28 XRD patterns of glass-ceramics (Zn-waste and clear cullet) sintered at 750°C

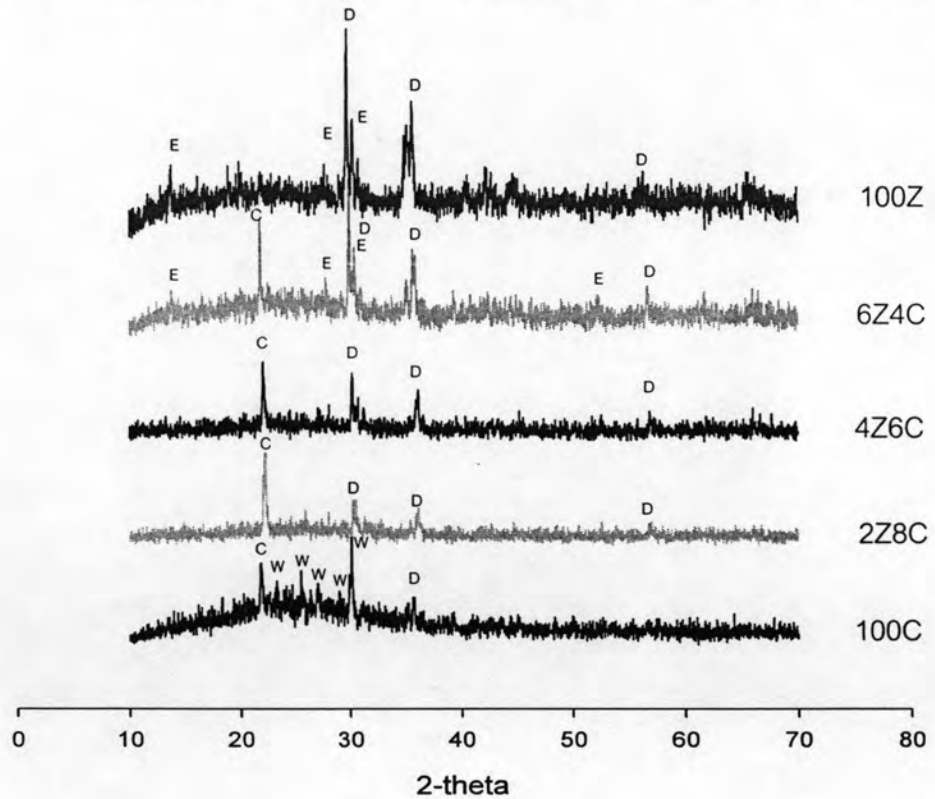W = Wollastonite   C = Cristobalite   D = Diopside   E = Esseneite,sodian

Fig. 4.29 XRD patterns of glass-ceramics (Zn-waste and clear cullet) sintered at 850°C

The presence of phases in glass-ceramics were a group of silicate materials (pyroxenes) such as diopside ($CaMgSi_2O_6$), wollastonite ($CaSiO_3$), and esseneite-sodian ((Ca,Na)(Fe,Mn,Zn)Si_2O_6). The difference of phase results from substitution of suitable ions in appropriate sites within the structure. General chemical formula of pyroxenes is $M2M1T_2O_6$ where M2 refer to cations distorted octahedral coordination, M1 to cations in a regular octahedral coordination, and T to tetrahedrally coordinated cations. The possible ions occupied in the M2, M1, and T site of pyroxene were shown in Fig. 4.30 [31].
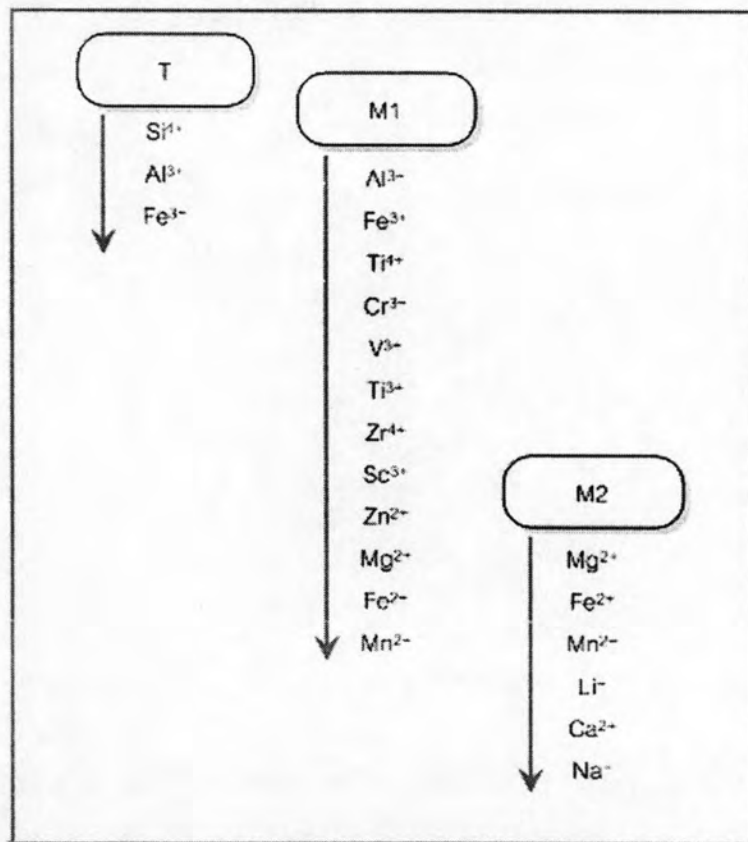

Fig. 4.30 Ideal sites occupancy of cations between the T, M1, and M2 sites of pyroxene [31]

The occupations of cations between the T, M1, and M2 sites of pyroxene depend on thermodynamic behavior [31,32], which are difficult to explain in this study. However, the substitutions of cations into their sites result in phase modification and there are effects on properties of specimens.

In the case of Zn-waste mixed with amber cullet, Fig. 4.31 and Fig. 4.32 are XRD results of the glass-ceramics sintered at $750^{\circ}C$ and $850^{\circ}C$, respectively. The specimens sintered at $750^{\circ}C$ showed an amorphous pattern similar to glass-ceramics contained Zn-waste mixed with clear cullet but the phases after heat treatment at $850^{\circ}C$ is different. It was found that wollastonite ($CaSiO_3$) is a major phase present in this sample. Diopside ($CaMgSi_2O_6$) and cristobalite (SiO_2) phases were occurred when Zn-waste was added into the composition. Moreover, it was also found that a peak of cristobalite (SiO_2) is an outstanding in the 2Z8A specimen then gradually decreased in 4Z6A and disappeared in 6Z4A specimen.

The difference phases present in glass-ceramics contained Zn-waste mixed with clear cullet and Zn-waste mixed with amber cullet results from different composition of raw materials. From Appendix E, it was found that glass-ceramics compositions in the group of amber cullet contained lower amount of MgO than that of clear cullet resulted in wollastonite ($CaSiO_3$) as a major phase in this mixture. This phenomena can be supported by previous study [33] reported that the content of MgO less than 3% in the compositions of glass-ceramics formed wollastonite as a major phase, when MgO increased (more than 3 wt%), diopside will gradually occur in the specimens.
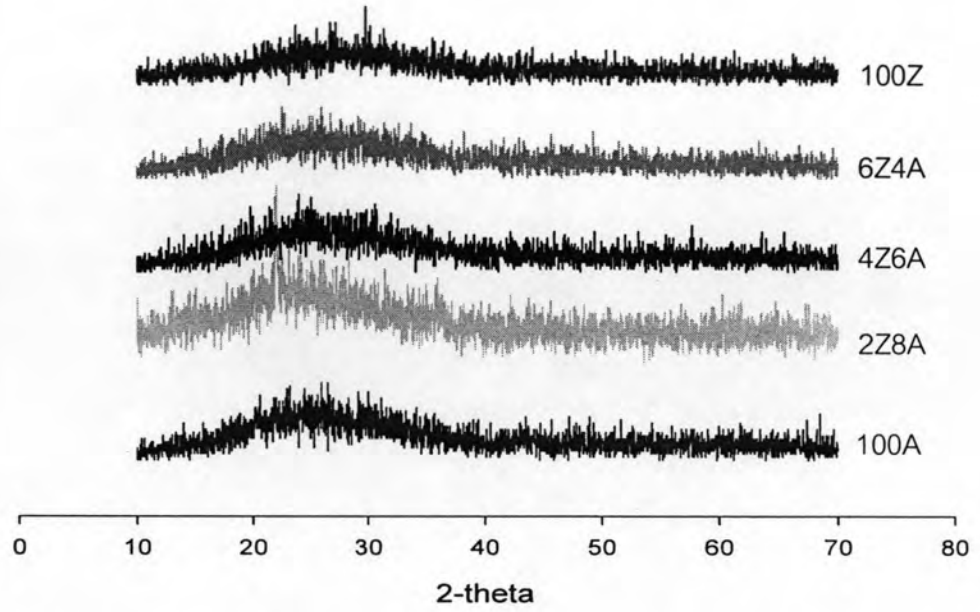
Fig. 4.31 XRD patterns of glass-ceramics (Zn-waste and amber cullet) sintered at 750°C

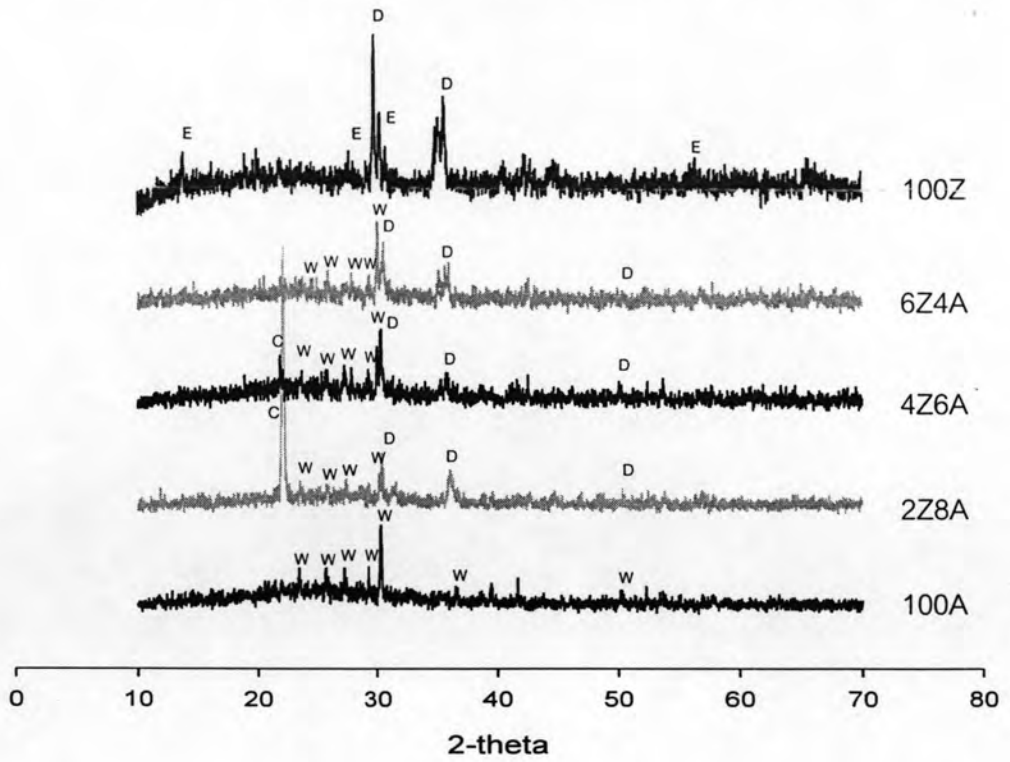W = Wollastonite   C = Cristobalite   D = Diopside   E = Esseneite,sodian

Fig. 4.32 XRD patterns of glass-ceramics (Zn-waste and amber cullet) sintered at 850°C
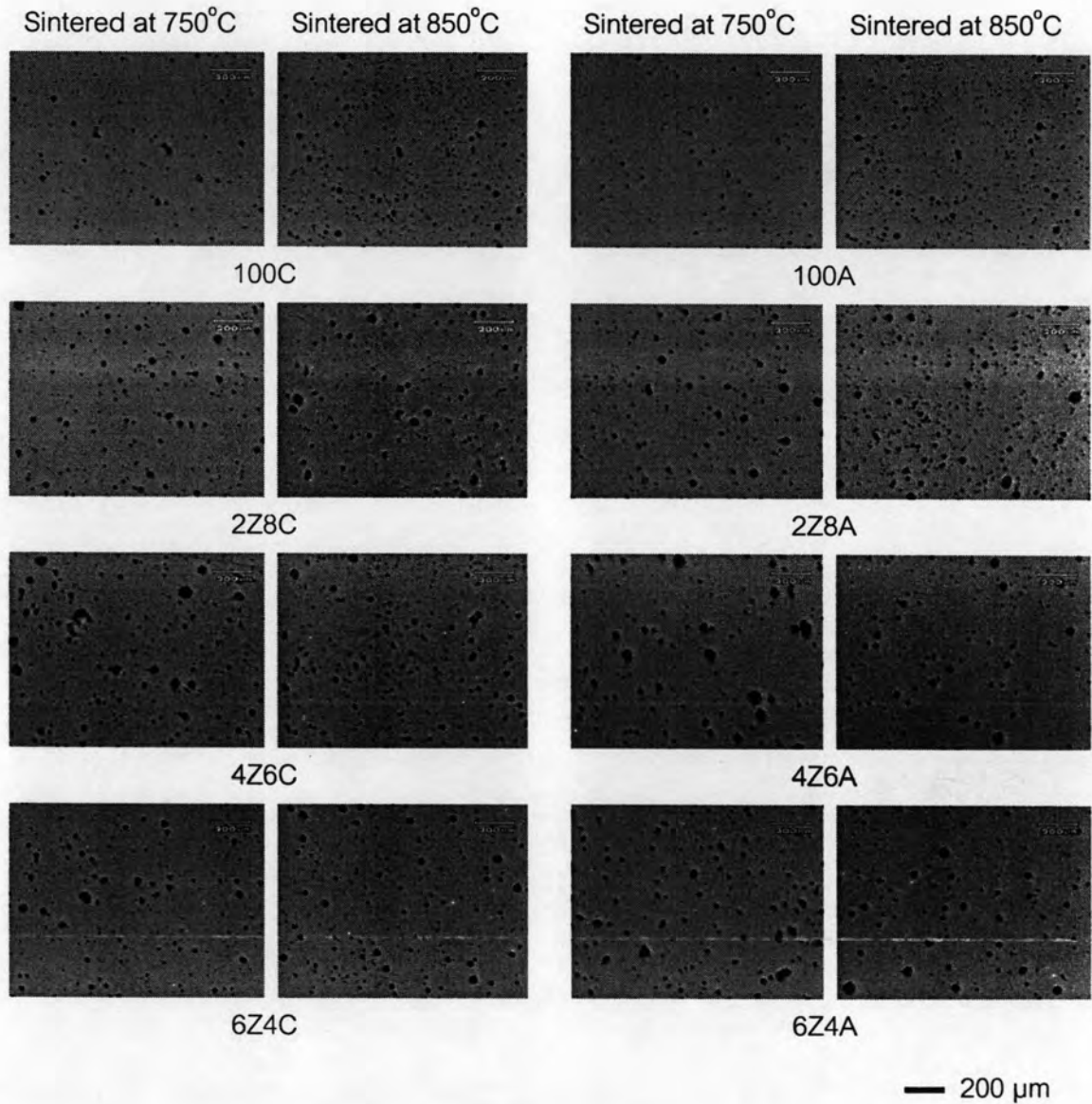
4.3.2.3 Microstructure

a) Optical images

Sintered at 750°C   Sintered at 850°C   Sintered at 750°C   Sintered at 850°C

100C   100A

2Z8C   2Z8A

4Z6C   4Z6A

6Z4C   6Z4A

— 200 μm

Fig. 4.33 Cross-section of glass-ceramics show pores

The cross-section of glass-ceramics were polished to obtained mirror-like surface to observe the porosities inside specimens using optical microscopy, OM. Fig. 4.33 shows fine pores in all specimens. It is note that glass-ceramics achieved by this process are superior density and less pores than glass-ceramics obtained from non-melting process.

b) <u>SEM</u>

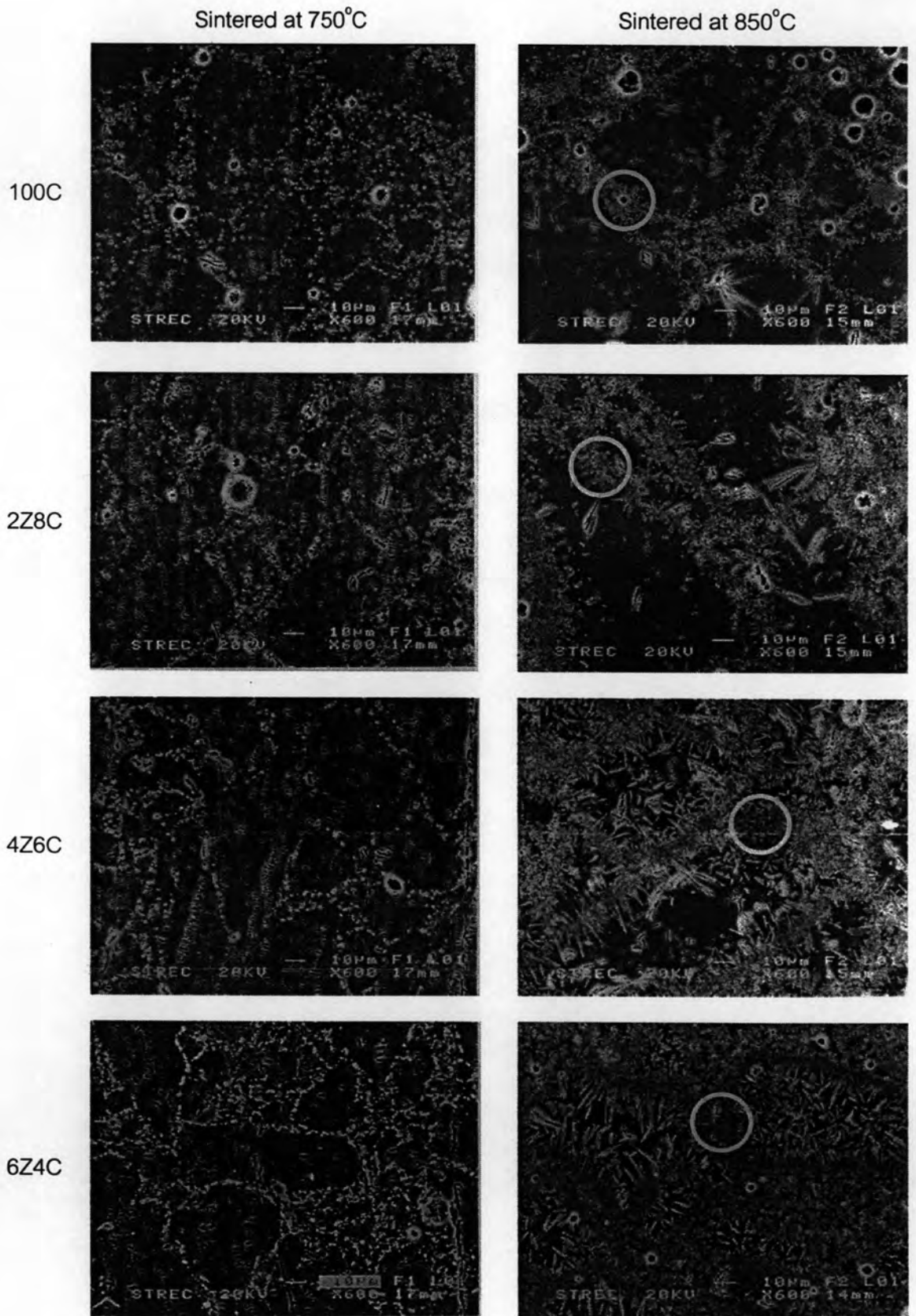| Sintered at 750°C	Sintered at 850°C

100C

2Z8C

4Z6C

6Z4C

Fig. 4.34 SEM images of glass-ceramics contained Zn-waste and clear cullet

The microstructures of glass-ceramics, Zn-waste mixed with clear cullet, observed using SEM is shown in Fig. 4.34. It was found that sample sintered at 750°C reveals an intermediate state of densification because the particle boundaries show continuous pore [9]. Furthermore, it was also found that crystal formation does not occur in this temperature in agreement with XRD. For sample sintered at 850°C, microstructures were evidenced for a final stage of sintering owing to closed and spherical pores located at particle boundaries. Moreover, crystal formations were able to behold in this sintering temperature by generate from particle boundaries. It is clearly found that the 6Z4C glass-ceramics were capable of forming the crystal easily which can be seen from numerous of crystals more than other glass-ceramics confirmed by image analysis. The percentage of crystal measured from Fig. 4.34 of 100C, 2Z8C, 4Z6C, and 6Z4C glass-ceramics is 22.34%, 46.06%, 68.77%, and 76.52%, respectively.
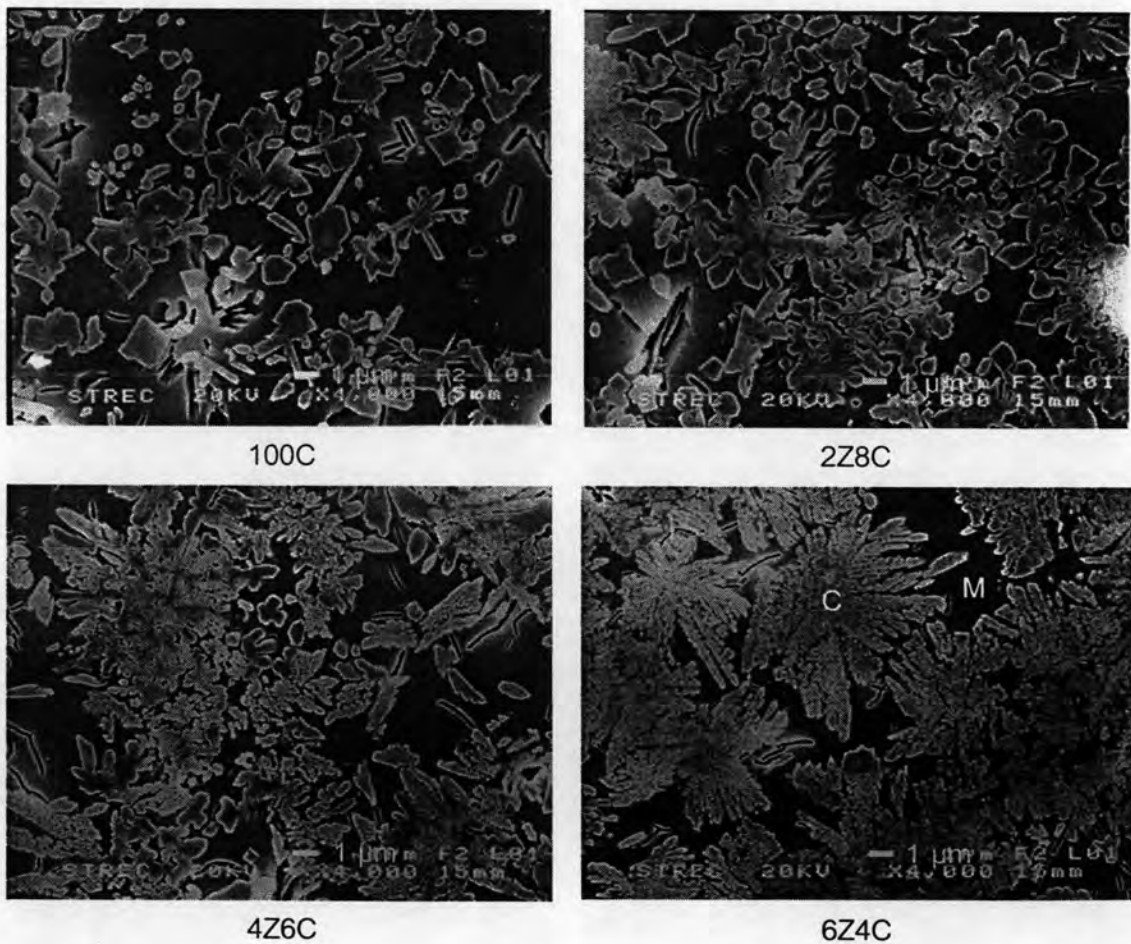

100C

2Z8C

4Z6C

6Z4C

Fig. 4.35 SEM images in the selected area of glass-ceramics at 850°C

The crystalline morphology in the selected area of each specimen in Fig. 4.34 is shown in Fig. 4.35. It exhibited the influence of Zn-waste in composition on the crystalline morphology. Increasing amount of Zn-waste from 20 wt%, 40 wt%, until 60 wt% gradually changed the morphology from the square shape to dendritic or arborescent crystals. The EDS analysis confirmed that the crystals (C point) are crystals in pyroxene (diopside ($CaMgSi_2O_6$) and esseneite-sodian ($(Ca,Na)(Fe,Mn,Zn)Si_2O_6$)) groups because it shows higher concentration of chemical element such as Ca, Mg, Na, Fe, Mn, and Zn than the matrix area (M point). The more dendritic crystals were arisen by increasing amount of Zn-waste because the replacement modified ions may reduce surface tension and decrease the viscosity, which favor the crystallization process [14,33]. The raw data of the EDS analysis can be seen in Appendix F.

The SEM images for glass-ceramics containing Zn-waste and amber cullet are shown in Fig. 4.36. The microstructure shows the same result as in the glass-ceramics with clear cullet. At sintering temperature of 750°C, the crystal was not form and continuous pore which is characteristic of intermediate state of densification. At 850°C, it can be seen that white crystals dispersed on the surface of specimens which resulted in inscrutable particle boundaries. However, at high magnification (Fig. 4.37), it was found that the white color is not crystal but it is needle-like pores. The presence of many needle-like pores may be generated by etching with HF because the major phase of glass-ceramics in the amber group is wollastonite ($CaSiO_3$) which is more soluble in acid than the glassy matrix [34].

In Fig. 4.37, the crystals of 100A glass-ceramics were hexagonal shape and gradually transformed to dendritic shape as Zn-waste percentage increased. The dentritic morphology of crystal formed in the group of amber cullet (Fig. 4.37) was different from that one in the group of clear cullet (Fig. 4.35) because the dissimilar chemical composition of glass-ceramics as shown in Appendix E resulted in different phase formation. The percentage of crystal increased with increasing amount of Zn-waste confirmed by image analysis. From Fig. 4.36, percent crystal of 100A, 2Z8A, 4Z6A, and 6Z4A glass-ceramics is 48.73%, 57.62%, 78.43%, and 84.13%, respectively.
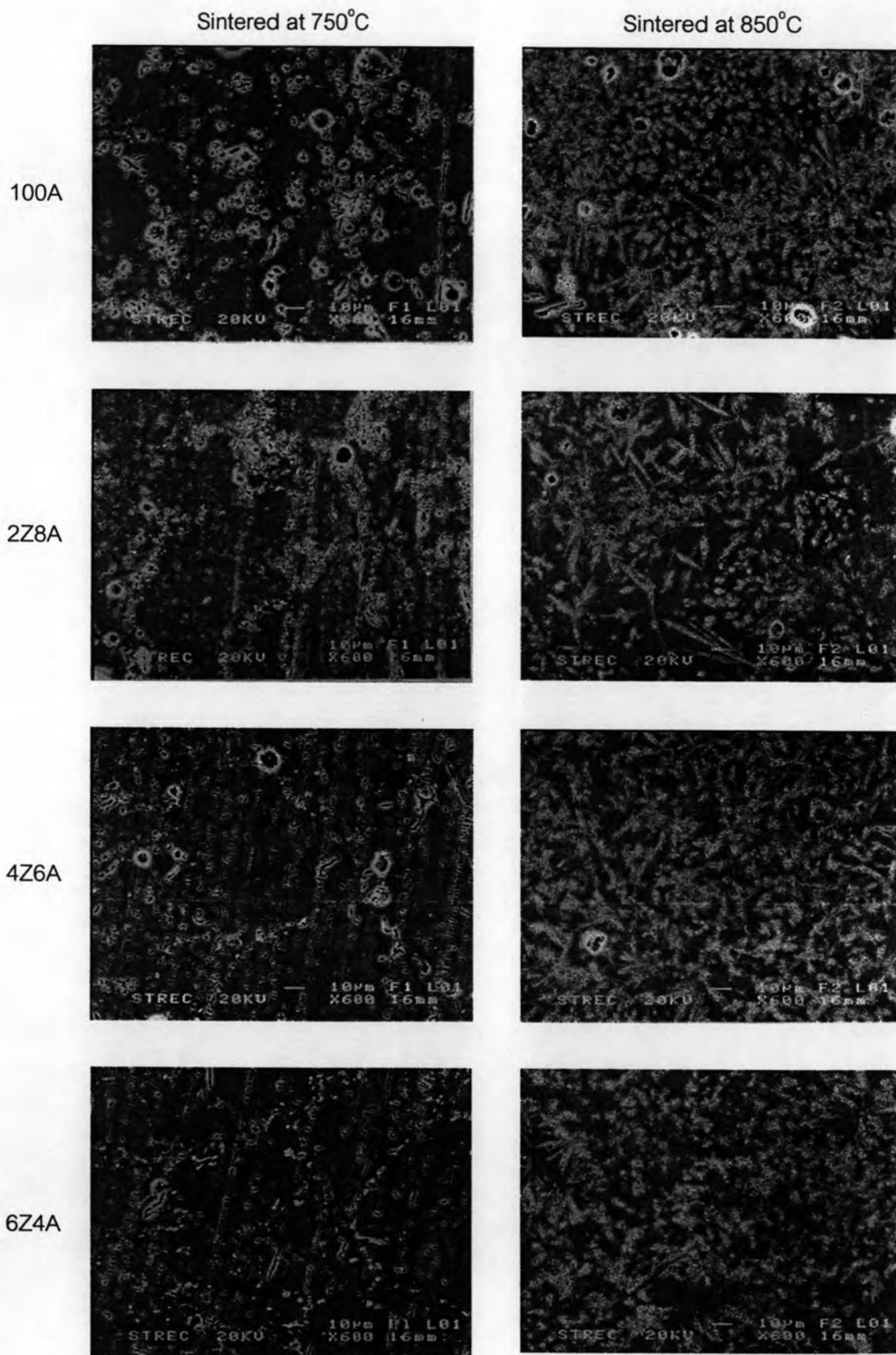
Sintered at 750°C   Sintered at 850°C

100A

2Z8A

4Z6A

6Z4A

Fig. 4.36 SEM images of glass-ceramics contained Zn-waste and amber cullet

Sintered at 750°C   Sintered at 850°C

100A   2Z8A
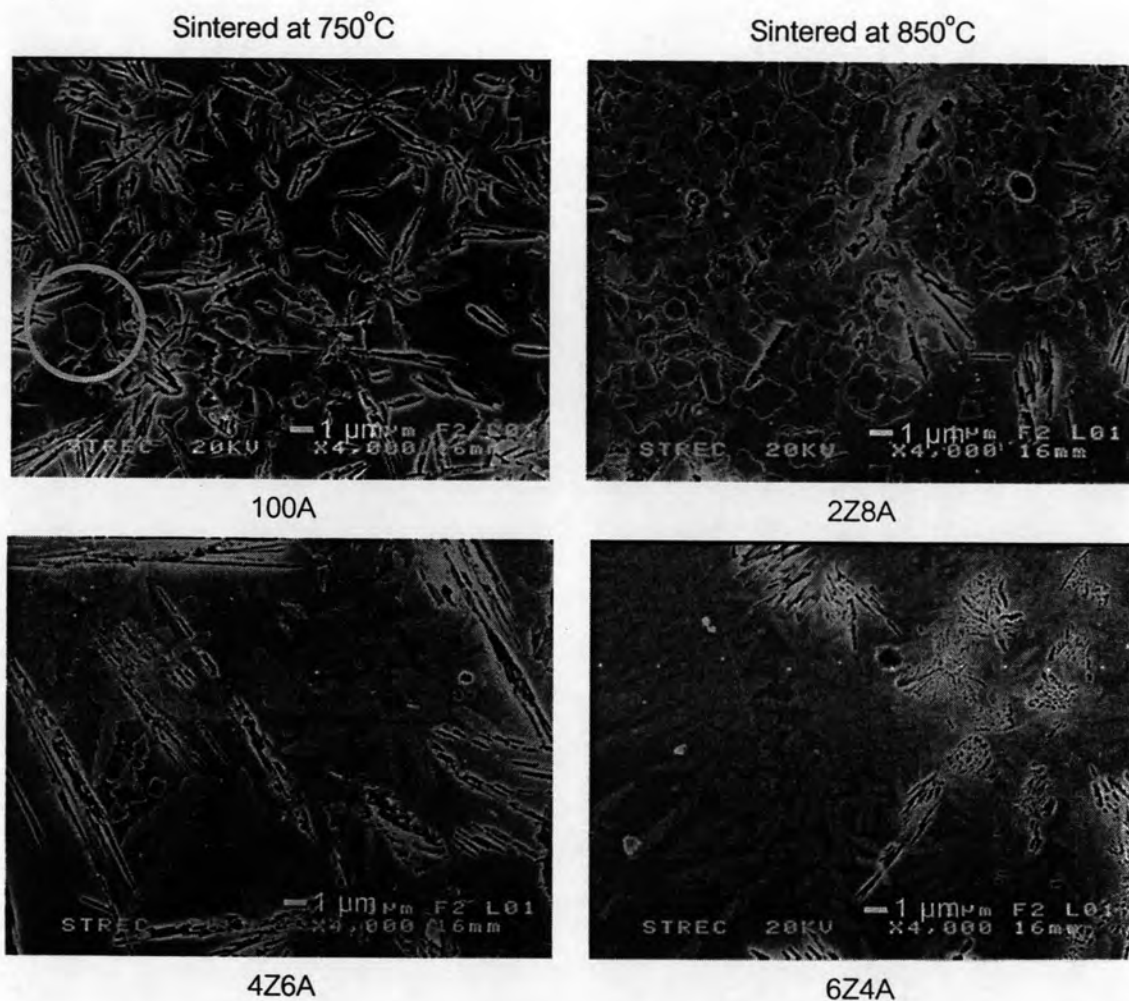
4Z6A   6Z4A

Fig. 4.37 SEM images in high magnification of glass-ceramics sintered at 850°C

From XRD results, wollastonite is a major phase for glass-ceramics in this group, hence, apparent crystal morphology may be characteristic of this phase. It can be supported by previous study [35] that there are various crystal morphologies of wollastonite phase such as hexagonal and dendritic shape which is corresponding to Fig. 4.37.

4.3.2.4 Mechanical properties

a) <u>Bending strength</u>

Strength of glass-ceramics was determined by three-point bending method. The bending strength of glass-ceramics from Zn-waste mixed with clear cullet and amber cullet are shown in Fig. 4.38 and Fig. 4.39, respectively.
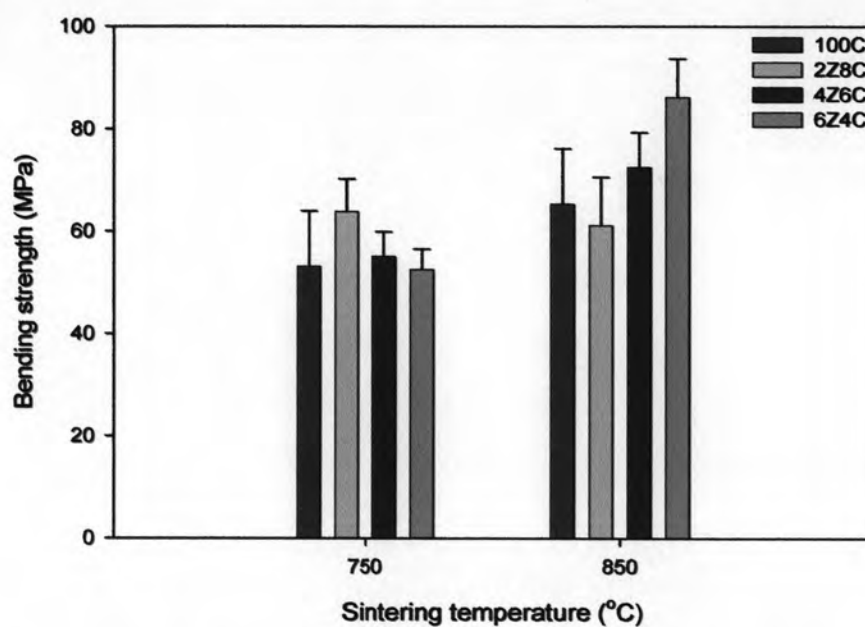

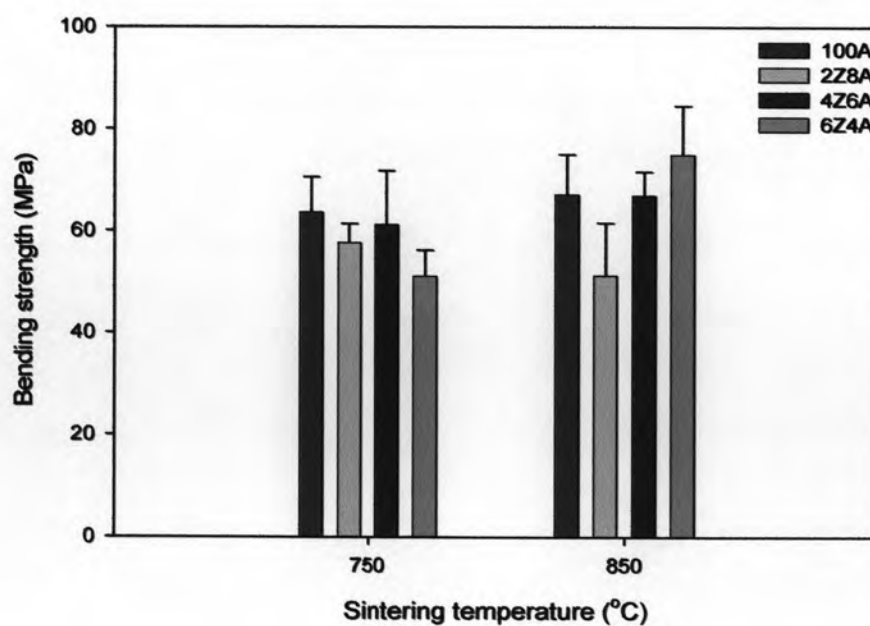Fig. 4.38 Bending strength of glass-ceramics with clear cullet

Fig. 4.39 Bending strength of glass-ceramics with amber cullet

The bending strength of all specimens sintered at 750°C was in the range of 52.5-63.8 MPa and increased to 61.2-86.5 MPa after sintering at 850°C. Specimens sintered at 750°C have lower strength than the specimens sintered at 850°C owing to the presence of amorphous phase. For the sample sintered at 850°C, the bending strength of glass-ceramics increased with increasing in sintering temperature and percentage of Zn-waste as a result of crystal formations. However, glass-ceramics containing 20 wt% of Zn-waste (2Z8C and 2Z8A) showed a drop of bending strength which may be resulted from crystal mismatch in the specimens.

The maximum strength of about 86.5 MPa obtained from 6Z4C glass-ceramics sintered at 850°C because it contained a large amount of crystals resulted in the superior strength. The effect of cullet types on the bending strength can be seen clearly in glass-ceramics sintered at 850°C. Glass-ceramics in the group of Zn-waste and clear cullet revealed the higher bending strength than that of the other. This phenomenon may be due to a property and type of phase formations in the specimens.

Normally, porosity has influence on the strength of glass-ceramics because they reduce the cross-section area. But in this study, all of the samples showed the similarity of size, shape, and pore distribution as shown in Fig. 4.33, thus, effect of porosities on the strength of glass-ceramics is very small. Therefore, crystal mismatch and a quantity of crystal play an important role on bending strength. The raw data of bending strength was shown in Appendix G.

All of specimens have strength higher than the minimum requirement of ISO 13006 for ceramic floor tiles (35 MPa for water absorption<0.5%), thus, glass-ceramics in this study are suitable for tiles production.
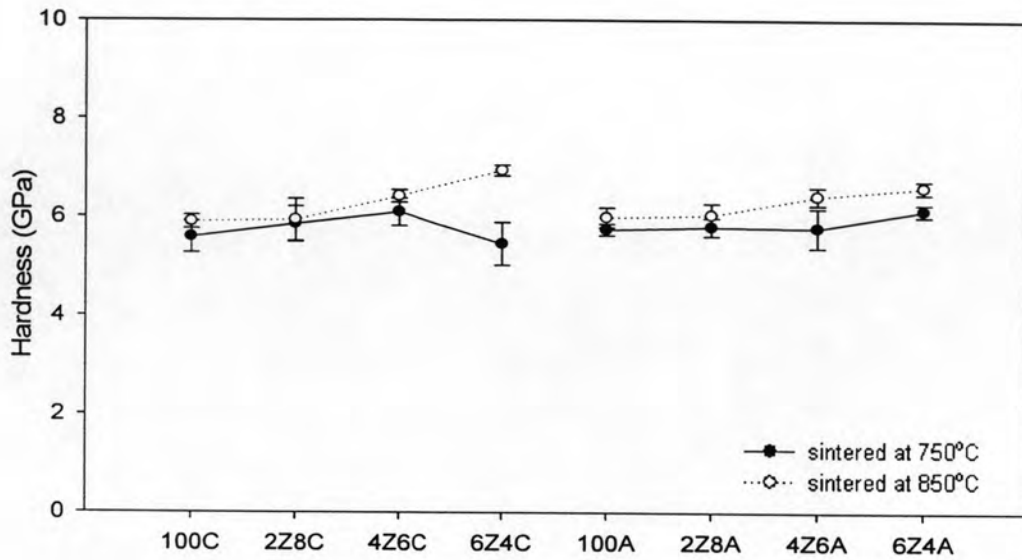
b) <u>Hardness</u>

Fig. 4.40 Hardness of glass-ceramics

The range of the Vickers hardness values were 5.45-6.14 GPa and 5.90-6.94 GPa for glass-ceramics sintered at 750°C and 850°C, respectively. It was found that hardness is a function of temperature and amount of Zn-waste. Hardness of glass-ceramics increased with increasing in sintering temperature and amount of Zn-waste. The Vickers hardness of obtained glass-ceramics in Mohs' hardness scale was about 5-6, thus, their hardness is sufficient for an application as wall tiles and floor tiles which require, in general, a Mohs' hardness of 5 [36]. The raw data of hardness of glass-ceramics and Mohs-Vickers hardness conversion [37,38] were shown in Appendix G and Appendix J, respectively.
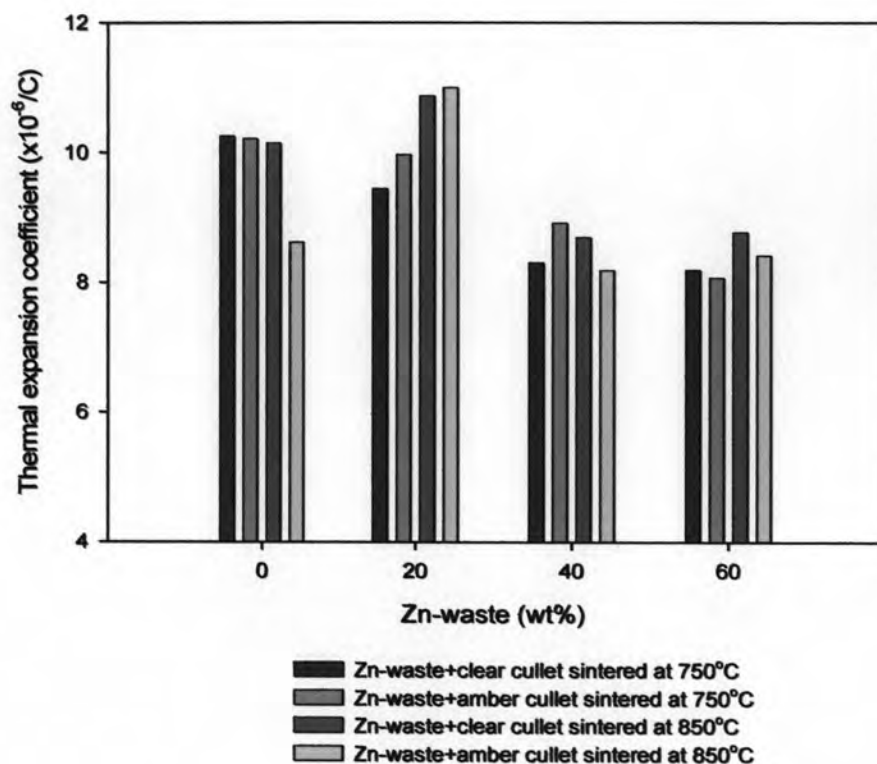
4.3.2.5 Thermal expansion coefficient

Fig. 4.41 Thermal expansion coefficient of glass-ceramics

Thermal expansions coefficient is shown in Fig. 4.41. It can be assumed that thermal expansion decreased with increasing quantity of Zn-waste in composition due to decreasing of alkali flux such as Na_2O which breaking up the oxygen bridges in glass [10]. However, the specimens of 2Z8C and 2Z8A sintered at $850^{\circ}C$ revealed the maximum thermal expansion coefficient because there is the cristobalite (SiO_2) as a major phase which has higher thermal expansion coefficient than diopside and wollastonite [33]. The raw data of thermal expansion coefficient of glass-ceramics was shown in Appendix H.

4.3.2.6 Chemical resistance

Chemical resistances were tested according to ASTM C650-97 [39] and the test result of the specimens heat-treated at 750°C and 850°C are shown in Table 4.4.

Table 4.4 Chemical resistances of glass-ceramics

Samples	Chemical		HB pencil
	HCl	KOH	
Sintered at 750°C			
100C	pass	pass	pass
2Z8C	pass	pass	pass
4Z6C	pass	pass	pass
6Z4C	pass	pass	pass
100A	pass	pass	pass
2Z8A	pass	pass	pass
4Z6A	pass	pass	pass
6Z4A	pass	pass	pass
Sintered at 850°C			
100C	pass	pass	pass
2Z8C	pass	pass	pass
4Z6C	pass	pass	pass
6Z4C	pass	pass	pass
100A	pass	pass	pass
2Z8A	pass	pass	pass
4Z6A	pass	pass	pass
6Z4A	pass	pass	pass

It was found that all specimens show good chemical resistance in both acid and base solutions. Also, pencil lines drawn on the surface can be removed easily with a damp cloth. Therefore, glass-ceramics produced in this study are suitable for tiles production.

4.3.2.7 Toxic leaching

In order to confirm that Zn-waste can be transformed into more stable materials like glass-ceramics in this study, the toxic leaching of heavy metal was tested following TCLP 1311 method. According to the standard of heavy metal leaching of the USA, the maximum concentration of contaminants for toxicity characteristic of Pb, As, and Cd were 5, 5 and 1 ppm, respectively [40].

Table 4.5 Toxic leaching of glass-ceramics sintered at 750°C and 850°C for 2 hours

samples	Toxic leaching (ppm)		
	Pb	As	Cd
Sintered at 750°C			
2Z8C	0.0810	< 0.05	0.003
4Z6C	0.1190	< 0.05	0.008
6Z4C	0.1700	< 0.05	0.009
Sintered at 850°C			
2Z8C	0.0600	< 0.05	0.007
4Z6C	0.0780	< 0.05	0.011
6Z4C	0.0880	< 0.05	0.009

Table 4.5 reported toxic leaching of glass-ceramics. It was found that the released Pb was varied from 0.06 – 0.17 ppm, As leaching was less than 0.05 ppm in every specimen, and Cd leakage was not over 0.011 ppm. All specimens have toxic leaching in the range allowed by the US regulations for heavy metal ions leaching. Therefore, it can be said that Zn-waste and glass cullet can be safely converted to tile products.

4.4 Effects of sintering time on physical and mechanical properties of glass-ceramics

4.4.1 Physical properties
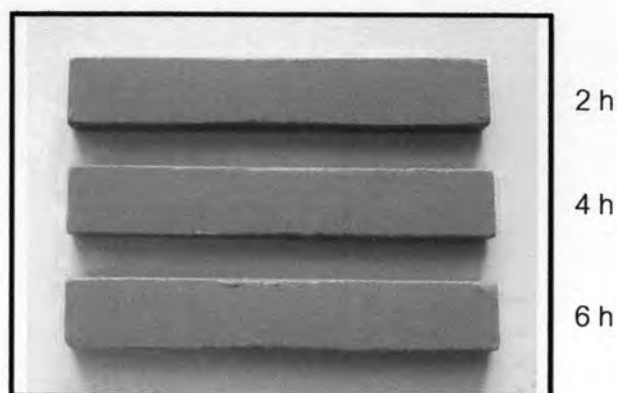
a) Visual observation

Fig. 4.42 6Z4C glass-ceramics from various sintering times

From Fig. 4.42, the shape of samples was still rectangular and not deformed. The appearance of surface converted from matt to glossy surface when increased crystallization times from 2 hours to 4 or 6 hours. Samples showed isotropic volume shrinkage because the ratio of volume shrinkage to linear shrinkage was about three times which can be seen in Fig. 4.43.
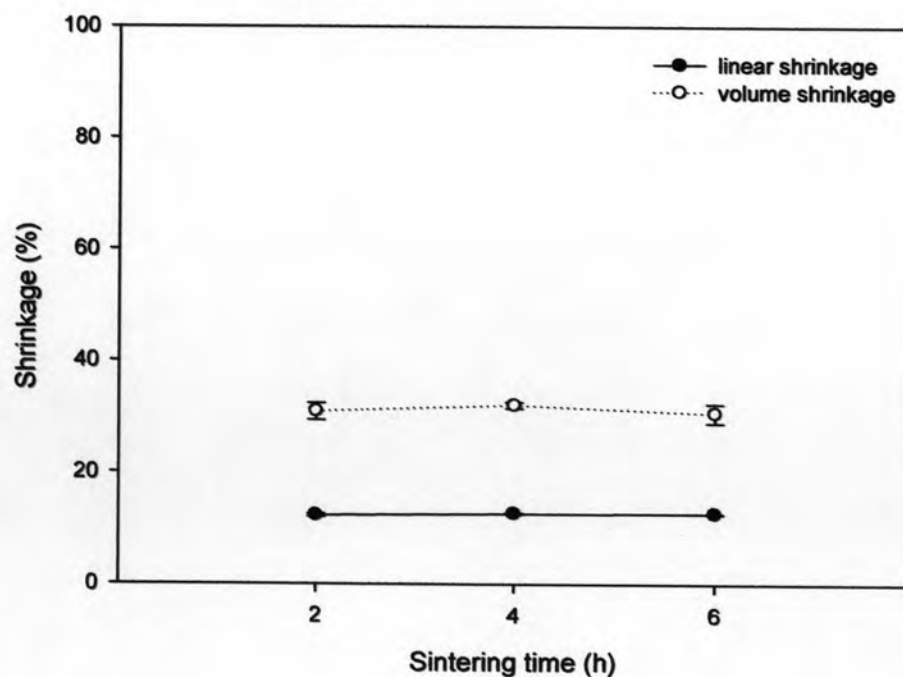

Fig. 4.43 Shrinkage of glass-ceramics sintered for various times

b) Apparent porosity, water absorption, and bulk density

Open pore can be closed after sintering for 2 hours confirmed by the near zero percent of apparent porosity and water absorption as shown in Fig. 4.44 and Fig. 4.45, respectively. Both figures indicate that after sintering, the water absorption is very low due to the near zero percent of apparent porosity.
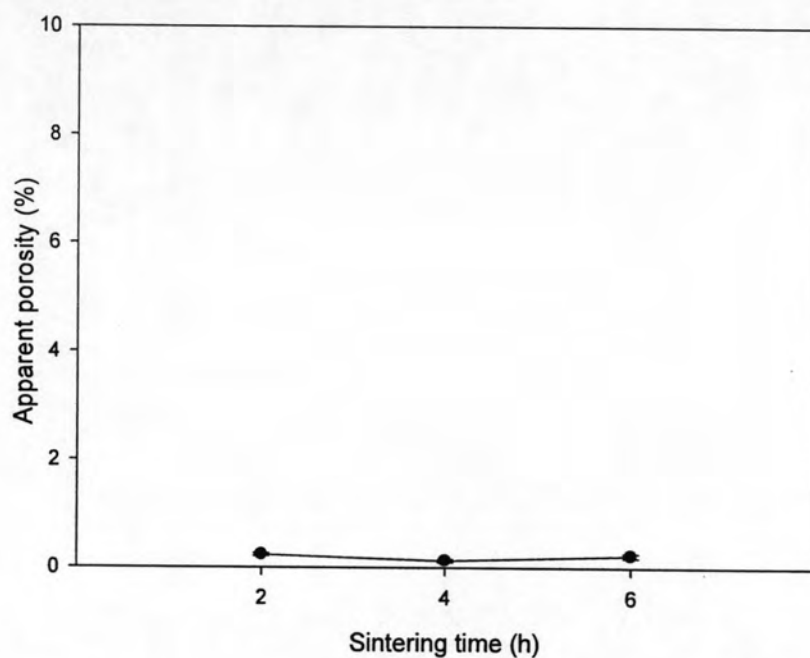

Fig. 4.44 Apparent porosity of glass-ceramics sintered for various times
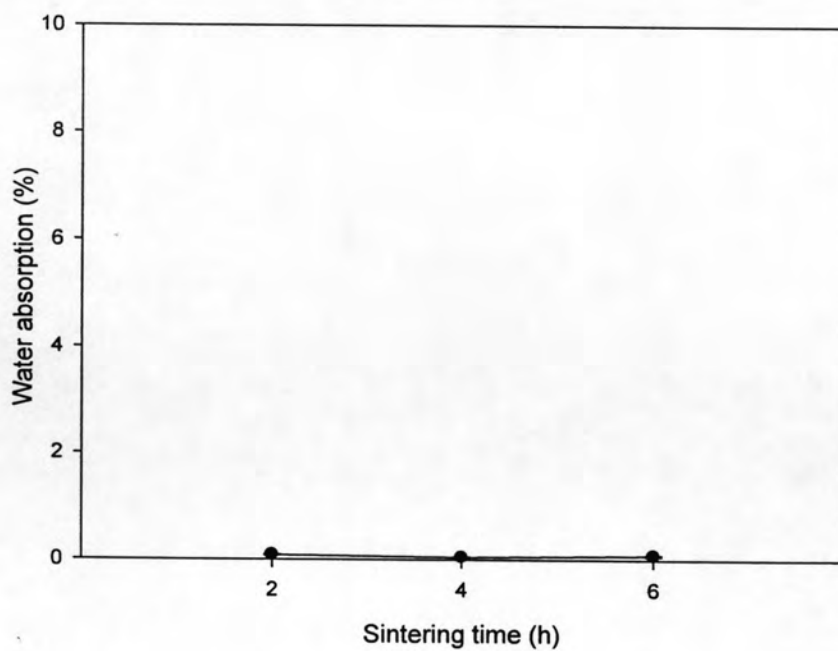

Fig. 4.45 Water absorption of glass-ceramics sintered for various times

Bulk density of glass-ceramics was plotted with sintering time in Fig. 4.46. The maximum bulk density about 2.83 g/cm^3 obtained from 6Z4C glass-ceramics sintered at 850°C for 2 hours and then slightly declined to 2.79 g/cm^3 for sintering time of 4 and 6 hours. Bulk density decreased with increasing sintering time, this behavior may be occurred from the increasing of crystal precipitations or growth of crystal and pores in the densification process [41].
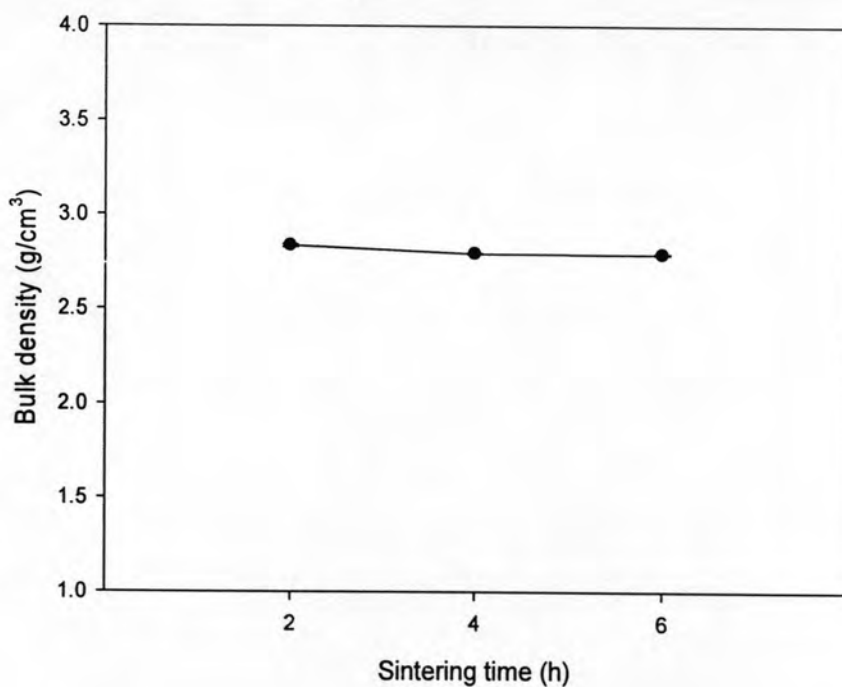

Fig. 4.46 Bulk density of 6Z4C glass-ceramics sintered for various times

However, decreasing of bulk density of 6Z4C glass-ceramics for sintering at various times is very small in comparing with glass-ceramics obtained from different composition (Fig. 4.27). It may be resulted from type and numbers of crystals were not so different in the same composition.

4.4.2 XRD patterns of glass-ceramics sintered for various times

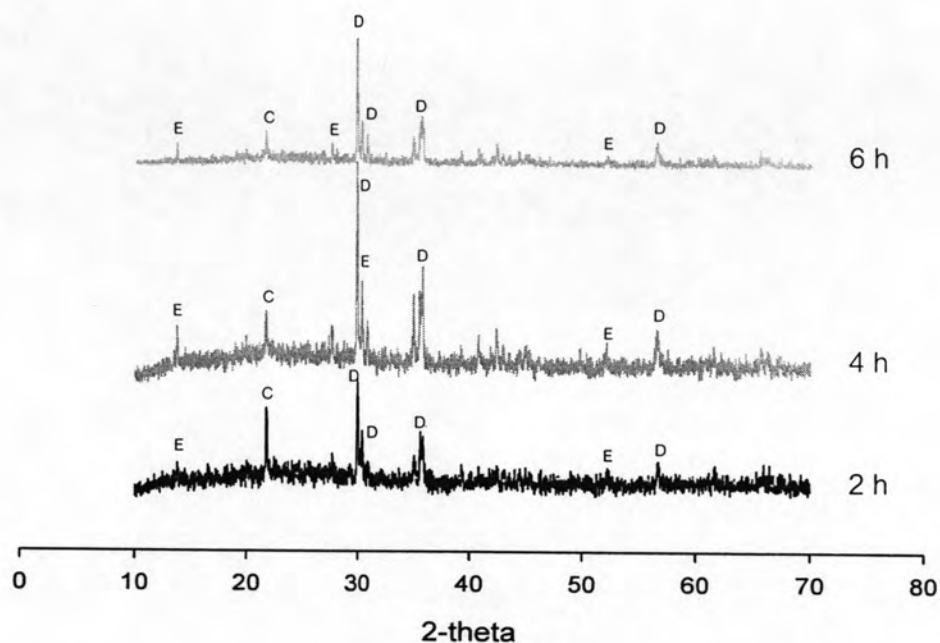C = Cristobalite   D = Diopside   E = Esseneite,sodian

Fig. 4.47 XRD pattern of 6Z4C glass-ceramics sintered for various times

The crystalline formations were investigated by the XRD and the result is shown in Fig. 4.47. The major phases are cristobalite (SiO_2), diopside ($CaMgSiO_2$), and esseneite, sodian (($Ca,Na)(Fe,Mn,Zn)Si_2O_6$). Moreover, it was found that the peak of esseneite, sodian (($Ca,Na)(Fe,Mn,Zn)Si_2O_6$) was outstanding after sintering for longer times. It is possible that the longer sintering time spent, the more modified ion (Na,Fe,Mn, and Zn) substituted into the structure of diopside ($CaMgSiO_2$) phase.
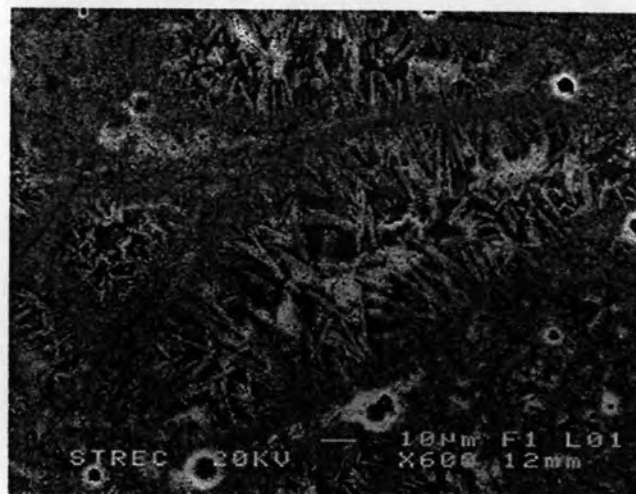
4.4.3   Microstructure of glass-ceramics sintered for various times
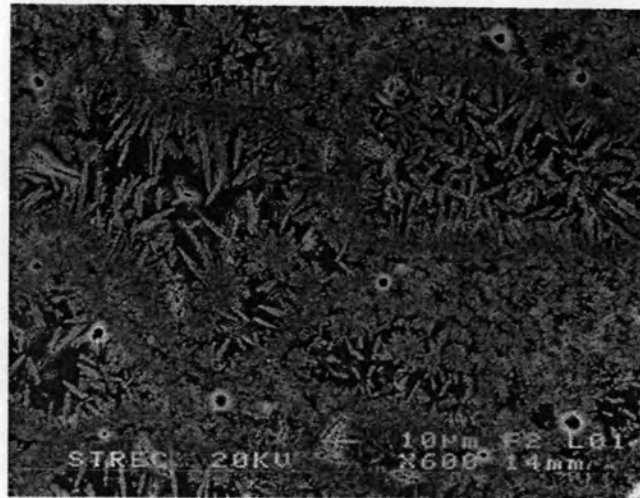
(a)
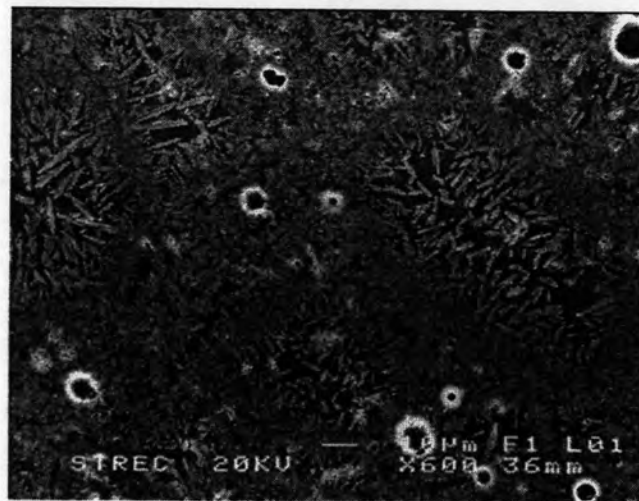
(b)

(c)

Fig. 4.48 SEM images of 6Z4C glass-ceramics sintered for 2 h (a), 4 h (b), and 6 h (c)

From Fig. 4.48, the 6Z4C glass-ceramics sintered at 850°C for 2 hours showed small spherical pores along the particle boundaries and the pore size increased with an increasing of sintering times. The morphology of crystalline is dendritic crystals and these characteristics belong to pyroxene group crystal confirmed by the EDS analysis. It was found that percent modified ions (Na, Fe, Mn, and Zn) increased while percentage of Ca and Mg decreased when sintering time was increased. The raw data of the EDS analysis are shown in Appendix F. Therefore, the EDS result was consistent with the XRD result that a number of esseneite, sodian $((Ca,Na)(Fe,Mn,Zn)Si_2O_6)$ phase increased when increased sintering times.

4.4.4 Mechanical properties of glass-ceramics sintered for various times

a) <u>Bending strength</u>
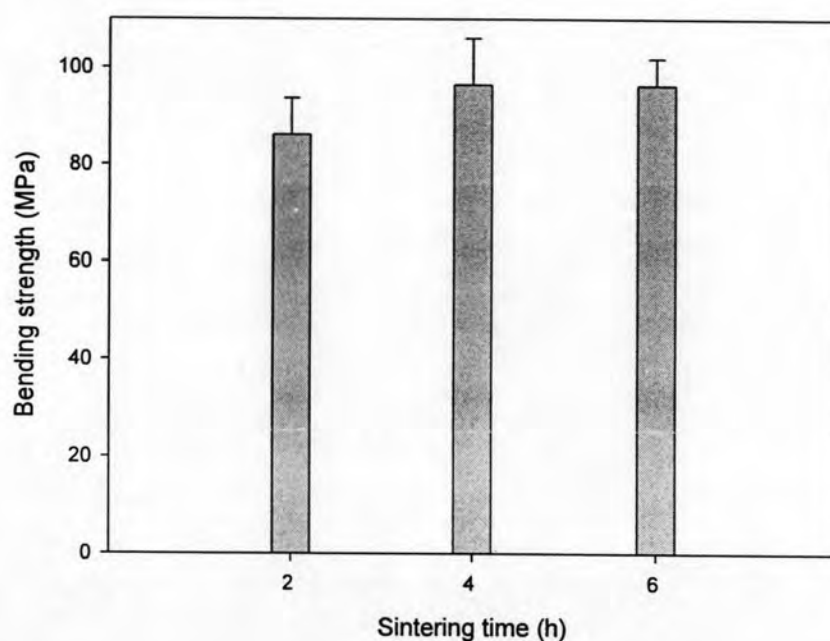

Fig. 4.49 Bending strength of 6Z4C glass-ceramics sintered for various times

From Fig. 4.49, it was found that the bending strength of sample increased from 86.5 MPa to 96.5 MPa when increased sintering time from 2 hours to 4 hours and bending strength was stable from 4 hours to 6 hours. The bending strength increased with increasing sintering time because of the rising amount of crystals.
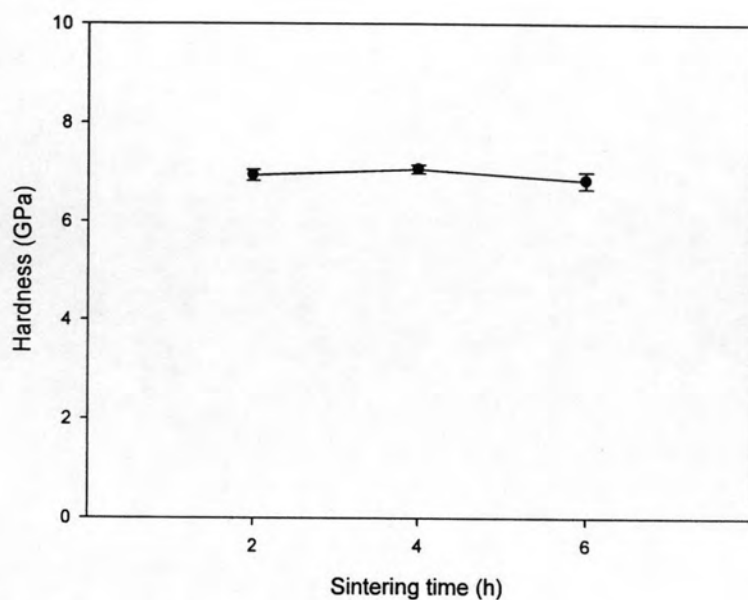
b) Hardness

Fig. 4.50 Hardness of 6Z4C glass-ceramics sintered for various times

The Vickers hardness of glass-ceramics shown in Fig. 4.50 has a value about 6.94, 7.06, and 6.83 GPa for sintering time of 2, 4, and 6 hours, respectively. The change of microstructure during crystallization resulted in the variation of the hardness [42].

4.4.5 Thermal expansion coefficient of glass-ceramics sintered for various times
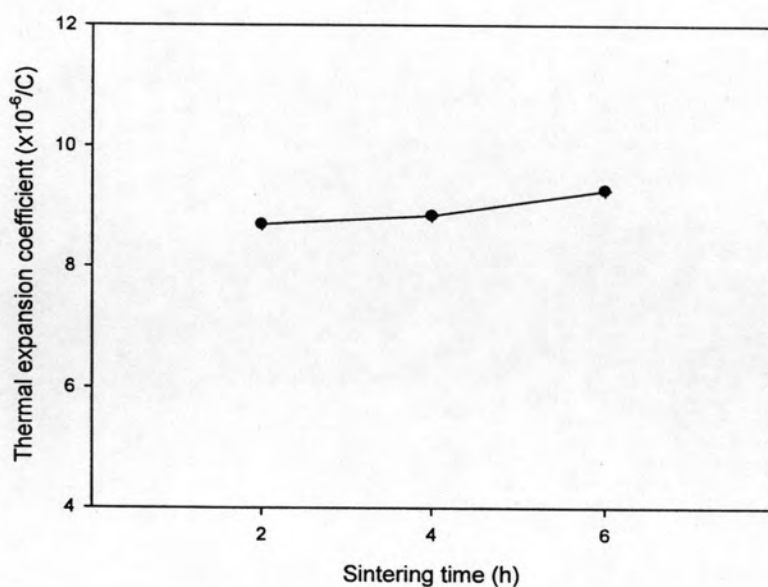

Fig. 4.51 Thermal expansion coefficient of 6Z4C glass-ceramics sintered for various times

The thermal expansion coefficient of 6Z4C glass-ceramics was increased gradually with an increasing in sintering time as shown in Fig. 4.51. The increase of thermal expansion coefficient of specimen sintered for a longer time resulted from a higher amount of Na in the crystal confirmed by EDS result as shown in Appendix F. Due to the substitution of Na in Ca site resulted in breaking up the oxygen bridges [10], thus, specimen give higher thermal expansion coefficient.

4.4.6 Chemical resistance of glass-ceramics sintered for various times

The several of sintering time does not affect on chemical resistance in every condition as shown in Table 4.6.

Table 4.6 Chemical resistances of 6Z4C glass-ceramics sintered at 850°C

Sintering time	Chemical		HB pencil
	HCl	KOH	
2 h	pass	pass	pass
4 h	pass	pass	pass
6 h	pass	pass	pass

4.4.7 Toxic leaching of glass-ceramics sintered for various times

Table 4.7 Toxic leaching of 6Z4C glass-ceramics sintered at 850°C

Sintering times	Toxic leaching (ppm)		
	Pb	As	Cd
2 h	0.0880	< 0.05	0.009
4 h	0.0880	< 0.05	0.020
6 h	0.0890	< 0.05	0.007

For the same condition as previous experiment, glass-ceramics with Zn-waste were tested for toxic leaching of heavy metal was tested following to TCLP 1311 method. The result of toxic leaching is shown in Table 4.7, all of the specimens revealed that the leaching of Pb, As, and Cd in the range allowed by the US regulations for heavy metal ions leaching. It can be noted that risky ion replaced other ions site and held in the framework of glass [43].

4.5 Application of glass-ceramics as an artificial marble

In order to expand the application of Zn-waste, artificial marble has been getting attention in this study. The attempt was made to imitate the natural marble by utilization of different color of glass-ceramics to produced wall tiles. The ratio of glass matrix (100C) to color glasses (100A, 2Z8C, 4Z6C, and 6Z4C) was 6:1. The various glass compositions were used to make different colors of artificial marbles.

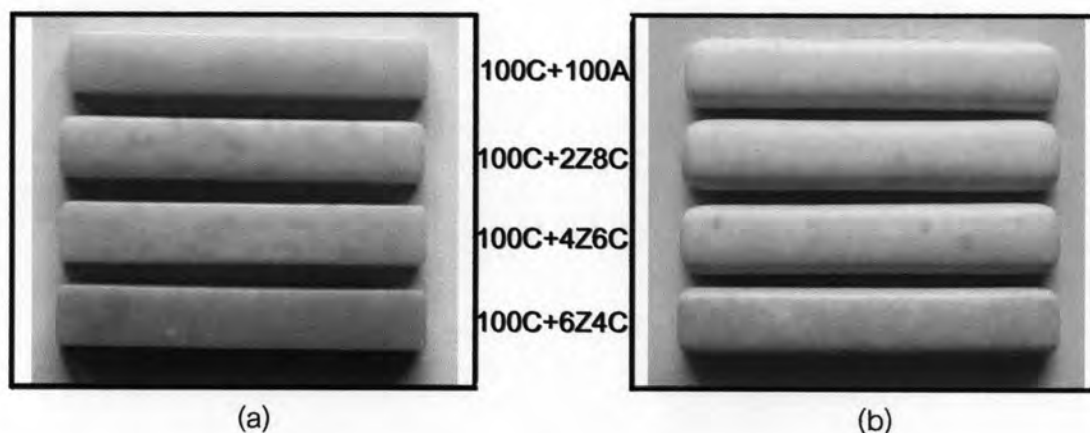### 4.5.1 Physical properties of the artificial marble

a) Visual observation

100C+100A

100C+2Z8C

100C+4Z6C

100C+6Z4C

(a)   (b)

Fig. 4.52 Artificial marble sintered at $750^{\circ}C$ (a) and $850^{\circ}C$ (b)

After sintering at $750^{\circ}C$ and $850^{\circ}C$, visual observation of artificial marble were shown in Fig. 4.52. Artificial marbles sintered at $750^{\circ}C$ show glossy surface and matt surface appeared at $850^{\circ}C$. The texture of the artificial marble looks like the natural marble and the colors depended on glass powder added. The mixtures of glass powder of 100C+100A, 100C+2Z8C, 100C+4Z6C, and 100C+6Z4C demonstrated yellowish, greenish, brownish, and darker brown, respectively.

b) Apparent porosity, water absorption, and bulk density

Apparent porosity and water absorption of artificial marble were close to 0 %, the raw data can be seen in Appendix I and lower than the Thai Industrial Standard of marble slabs (<0.2%).

As shown in Fig. 4.53, bulk density decreased when the sample was sintered at higher temperature. The raw data of bulk density of artificial marble was also shown in Appendix I. The approximation of bulk density of artificial marble sintered at 750°C and 850°C were 2.5 g/cm^3 and 2.45 g/cm^3, respectively. Comparing with Thai Industrial Standard of marble slabs, the bulk density of obtained artificial marble was higher than the standard (2.3 g/cm^3).

In consequence, physical properties of artificial marbles produced in this study passed the Thai Industrial Standard of marble slabs. It is shown that the texture and color of the artificial marble is resembled to the natural marble.
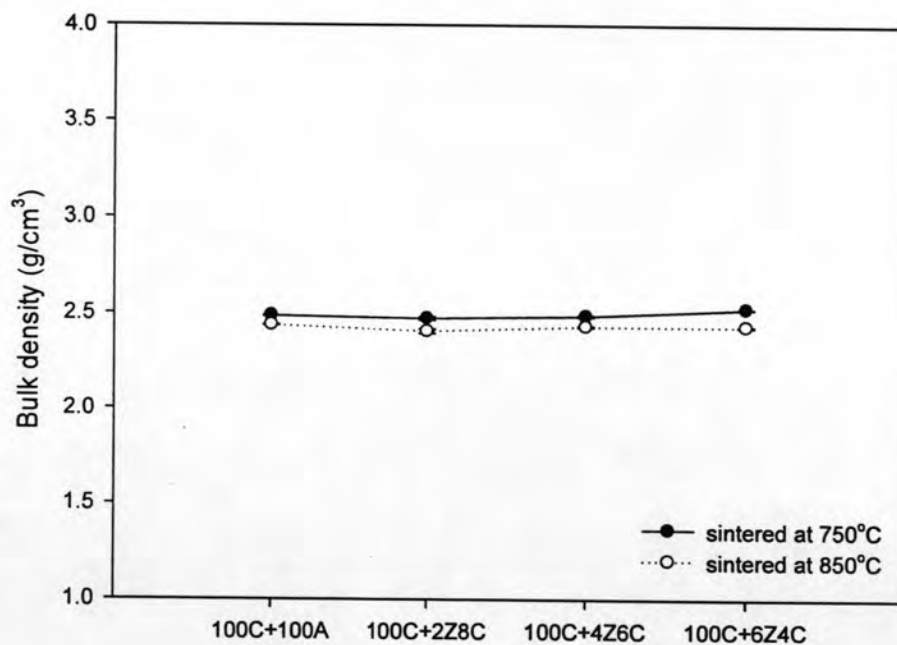
Fig. 4.53 Bulk density of artificial marble

4.5.2 Microstructure of the artificial marble

a) Optical microscope

Sintered at 750°C   Sintered at 850°C

100C+100A

100C+2Z8C
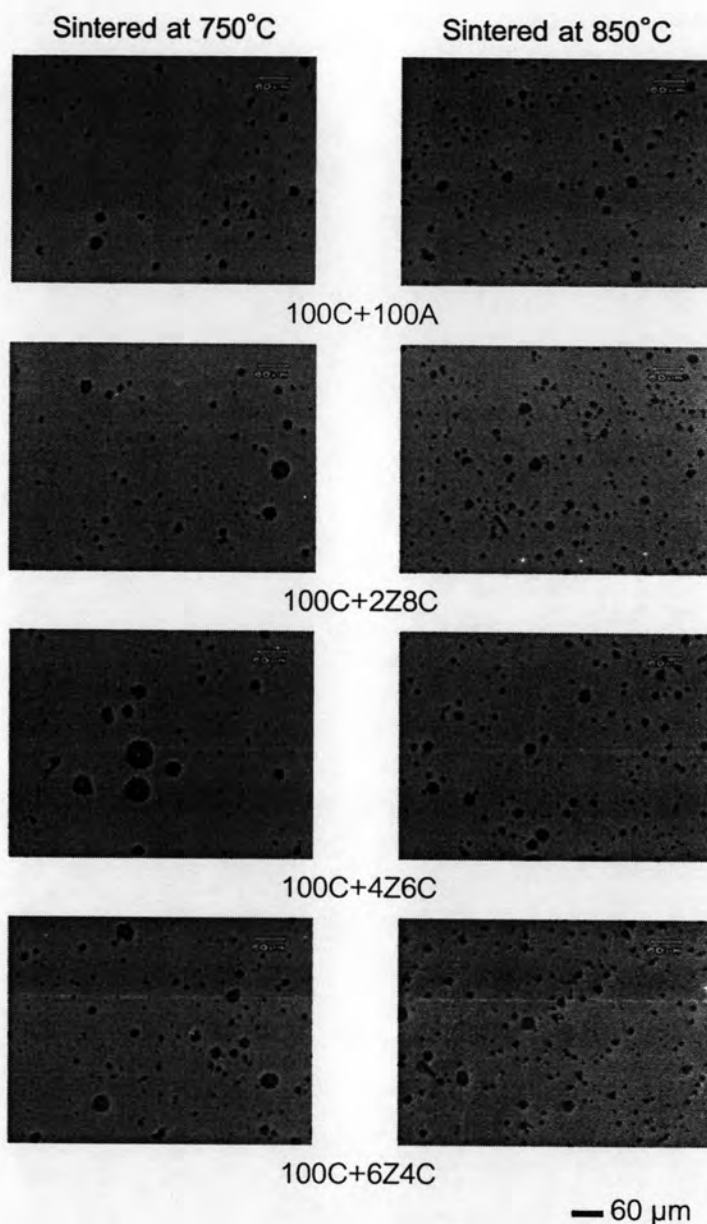

100C+4Z6C

100C+6Z4C

━ 60 μm

Fig. 4.54 Cross-section of artificial marble show pores

The microstructure of the artificial marble observed by an optical microscope can be seen in Fig. 4.54. Artificial marbles sintered at 850°C showed higher porosity than that of sintered at 750°C. The increasing amount of pores became higher after heat treatment at high temperature because of a mechanism for materials transport in order to get densification of specimens, like a result in section 4.2.2. Moreover, increasing of pore resulted in decreasing of bulk density as shown in Fig. 4.53.

4.5.3   Mechanical properties of the artificial marble
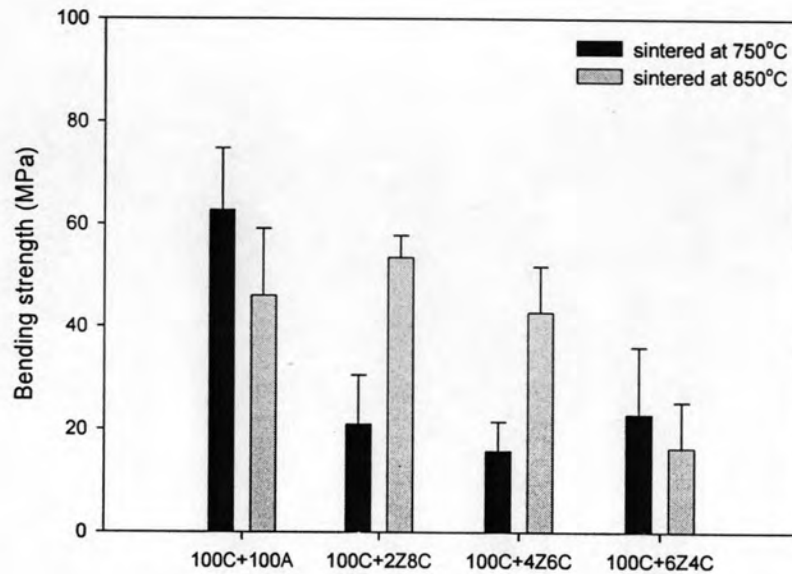
a)   <u>Bending strength</u>

Fig. 4.55 Bending strength of artificial marble

The bending strength of the artificial marble was shown in Fig. 4.55. The maximum strength was about 62.7 MPa obtained from 100C+100A sintered at 750°C and the minumum strength was about 15.83 MPa obtained from 100C+4Z6C sintered at 750°C. Compared with glass-ceramics in section 4.3, the bending strength of artificial marbles was lower than them. However, the bending strength of artificial marbles is sufficient high enough to satisfy the requirement for natural granite and marble which are 15 and 11-17 MPa [44], respectively. The raw data of bending strength of artificial marble was shown in Appendix I.
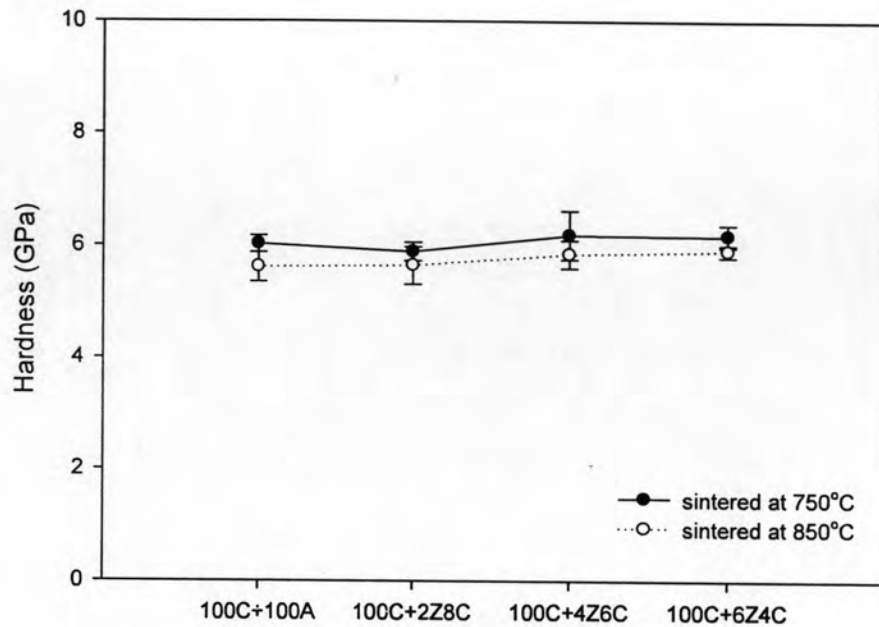
b) <u>Hardness</u>

Fig. 4.56 Hardness of artificial marble

The hardness of artificial marble can be seen in Fig. 4.56. Artificial marble sintered at 850°C showed lower hardness than sintering at 750°C. It may be resulted from microstructure change during crystallization resulted in drop of the hardness. The range of Vickers hardness of artificial marbles sintered at 750°C was 5.90-6.19 GPa and artificial marbles sintered at 850°C was 5.61-5.90 GPa which is about 5 Mohs scale. Approximation of the Vickers hardness to Mohs scale can be seen in Appendix J.

In general, the Mohs hardness of natural granite and natural marble are 5-6 and 3-5 [44], respectively. Therefore, Zn-waste and glass cullet can be converted to artificial marble which look like natural granite and marble. The texture and color of the artificial marble are similar to natural marble and their properties are equivalent to that of the natural marble.

4.5.4 Chemical resistance of the artificial marble

Table 4.8 Chemical resistances of the artificial marble

Samples	Chemical		HB pencil
	HCl	KOH	
Sintered at 750°C			
100C+100A	pass	pass	pass
100C+2Z8C	pass	pass	pass
100C+4Z6C	pass	pass	pass
100C+6Z4C	pass	pass	pass
Sintered at 850°C			
100C+100A	pass	pass	pass
100C+2Z8C	pass	pass	pass
100C+4Z6C	pass	pass	pass
100C+6Z4C	pass	pass	pass

Artificial marbles were tested for chemical resistance followed ASTM C650-97 and the result is shown in Table 4.8. All of the specimens passed the test in every condition.